Data Quality Analysis of the Leica SPL100

Airborne Single Photon Lidar Sensor

A Thesis

Presented to

the Faculty of the Department of Civil and Environmental Engineering

University of Houston

In Partial Fulfillment

of the Requirements for the Degree

Master of Science

in Geosensing Systems Engineering and Sciences

by

Rebecca A. Brown

August 2019

Data Quality Analysis of the Leica SPL100 Airborne Single Photon Lidar Sensor

_____

Rebecca A. Brown

Approved:

_____
Chair of the Committee
Craig L. Glennie, Ph.D.
Associate Professor
Civil and Environmental Engineering

Committee Members:

_____
Preston Hartzell, Ph.D.
Research Assistant Professor
Civil and Environmental Engineering

_____
Hyongki Lee, Ph.D.
Associate Professor
Civil and Environmental Engineering

_____
Zhigang Pan, Ph.D.
Geoscientist
Leica Geosystems

_____
Suresh K. Khator, Ph.D.
Associate Dean
Cullen College of Engineering

_____
Craig L. Glennie, Ph.D.
Program Director
Geosensing Systems Engineering and Sciences

Acknowledgments

In loving memory of my mother, my first teacher. Special thanks are also given to my family and friends who supported me. The path to completing this thesis was not a journey I could undertake alone. Much appreciation is given to my boyfriend, Tim Capps, who has lightened the load I have I had to carry. I am also grateful for the many edits and suggestions from Dr. Preston Hartzell, who has greatly improved my research.

Data Quality Analysis of the Leica SPL100

Airborne Single Photon Lidar Sensor

An Abstract

of a Thesis

Presented to

the Faculty of the Department of Civil and Environmental Engineering

University of Houston

In Partial Fulfillment

of the Requirements for the Degree

Master of Science

in Geosensing Systems Engineering and Sciences

by

Rebecca A. Brown

August 2019

Abstract

Recently, Geiger-mode and single photon lidar sensors have emerged on the commercial market, advertising greater collection efficiency than traditional linear mode lidar systems. Non-linear photon detection is a new technology for the geospatial community, and its performance characteristics for surveying and mapping are not yet well understood. The goal of this thesis, therefore, is to examine the geospatial quality of the data produced by one of these new sensors, the Leica SPL100. The SPL100 was shown to have a lower ranging precision than linear lidar and that its precision is more negatively affected by surface properties such as low intensity, roughness, and slope. The accuracy of the SPL100, however, was found to be comparable to that produced by linear lidar for smooth horizontal surfaces. It was also observed that the post-processed SPL100 data has limited ability to resolve multiple returns through vegetation due to the current filtering algorithms employed.

Table of Contents

List of Figures

List of Tables

1. Introduction

Airborne lidar (Light Detection and Ranging) systems have become a ubiquitous surveying instrument for a variety of applications, including high-resolution mapping, earth sciences, forestry, bathymetry, and even archaeology [1], [2]. The basic underlying principle of lidar is the ability to precisely measure the travel time of light to calculate distance, or range. Traditionally, this has been done with linear mode lidar (LML) systems, which require hundreds to thousands of photons to achieve a single range measurement. Recent advances have brought new technologies to the commercial market in the form of single photon lidar (SPL) and Geiger-mode lidar (GML), which are systems that maximize collection efficiency using detectors that are sensitive to individual photons. In contrast to LML, such systems can achieve range measurements with just a few photons. SPL and GML systems can collect data at faster rates and with a lower cost than LML sensors [3]–[5]. However, given their recent release to the commercial market, the performance characteristics of these systems are not yet fully understood and are therefore examined in this work. In particular, this thesis focuses on the performance of the Leica SPL100, a single photon system that was released commercially in 2017. The Leica SPL100 is marketed as an ideal system for large area terrain mapping, e.g., collections on a county and state-wide scale [3], [6].

1.1 Leica SPL100 Lidar System

The SPL100 derives much of its heritage from NASA's Microlaser Altimeter or "microaltimeter," which, in 2001, demonstrated the first proof-of-concept of airborne photon-counting [3], [7]. The microaltimeter established the use of a 532 nm Nd:YAG

laser, which was chosen because the high efficiency commercial off-the-shelf sensors that were needed for single photon detection were limited to peak sensitivities in the visible wavelengths [3], [7]. Later generations of SPL systems, developed by Sigma Space, split the outgoing pulse to create a 10 x 10 array of "beamlets" that would then be received with an array of detector elements [3], [7], [8]. The High-Resolution Quantum Lidar System (HRQLS) and HRQLS-2 prototypes, which were the precursor to the SPL100, were completed in 2013 and 2016, respectively [3]. These systems were designed to fly at moderate altitudes and to map larger areas more quickly while still allowing the point density to be adjusted for individual needs [3], [7].

In 2016, Hexagon/Leica Geosystems acquired Sigma Space, and in 2017 the commercial release of the SPL100 (Figure 1) was announced [9], [10]. By splitting a single laser beam into a 10x10 array of low energy beamlets, the SPL100 can collect up to 6 million points per second with a 60 kHz pulse repetition frequency (PRF). On return, these beamlets are detected with sensors sensitive enough to detect individual photons. The SPL100's higher efficiency does come at the cost of reduced ranging precision and higher measurement noise from false returns, however [11], [12].

Figure 1: Leica SPL100 597 L x 508 W x 454 H mm (~1/5 scale)

Although not the focus of this thesis, a similar technology, Geiger-mode lidar, has been in development at the Massachusetts Institute of Technology, Lincoln Laboratory since the 1990s [13]. Until recently, GML was primarily used by various federal agencies for defense purposes. With assistance from DARPA, GML has been commercially available since 2015 through Harris Corporation's IntelliEarth system [4], [13]. There are several key differences between the GML and SPL systems. First, the SPL systems utilize commercial off-the-shelf photomultipliers while the IntelliEarth instead uses a relatively more expensive 32 x 128 array of single avalanche photodiodes (SAPDs) [3], [13], [14]. Although the IntelliEarth and SPL100 both have an array of detectors, the IntelliEarth outputs a single large laser spot, in contrast to the SPL100, which uses a diffractive optical element to split a highly collimated laser pulse into an array of beamlets [3], [4], [13]. Finally, these different technologies also operate at different laser wavelengths: the SPL systems in the visible spectrum at 532 nm and the IntelliEarth in the near-infrared (NIR) at 1064 nm [3], [4], [13].

1.2 Performance Evaluation

Given the SPL100's entry into the commercial sector just a few years ago, there is a paucity of peer-reviewed literature that has quantitatively evaluated its performance. Of the published studies available, Stoker et al. (2016) and Mandlburger et al. (2019) present the most rigorous analysis of data quality [4], [15]. There are, however, several authors that have given conceptual comparisons between LML, GML, and SPL, such as Ullrich and Pfennigbauer (2016, 2018) and Jutzi (2017) [11], [12], [14]. Additionally, researchers at Sigma Space have discussed the historical development of their SPL sensors in several

papers [3], [7], [8]. Degnan (2016) presented an overview of the HRQLS system design and expected performance characteristics derived from theoretical modeling [3].

A notable weakness of the available literature stems from the fact that most of the studies comparing the performance of SPL and LML systems examined data acquired with HRQLS, the precursor to the SPL100, e.g. Degnan (2016), Kim et al. (2015), Stoker et al. (2016), Swatantran et al. (2016) [3]–[5], [16]. Few studies have used the Leica SPL100, e.g., Mandlburger et al. (2019) [15]. Therefore, one of the goals of this thesis is to present an analysis of SPL100 data quality that takes into account the improvements that have been made in system design, system operation, and data processing in the intervening years. Additionally, the review presented here is more thorough and comprehensive than any previous study on the SPL100.

The relative accuracy of the SPL100 has been shown to be adequate for most applications, with point densities that generally surpasses LML [3]–[5], [15]. Given its operational efficiency, the SPL100 is well-suited for applications that require mapping large areas. In their evaluation of the HRQLS's ability to meet the needs of the 3D Elevation Program, Stoker et al. (2016) found that non-vegetated vertical accuracies were well within the USGS Lidar Base Specification v1.2 specifications[1] for both quality levels 1 and 2, but raised concerns about point densities and vertical accuracy in dense canopy for QL1/2 [4], [17]. Mandlburger et al. (2019), using the SPL100, concluded that the system is capable of moderate vegetation penetration and similar precision to LML over flat, smooth horizontal surfaces. The LML system, however, provided better ground

[1] USGS Lidar Base Specification: https://pubs.er.usgs.gov/publication/tm11B4

coverage under tree canopies and its precision was considerably better over sloped and grassy surfaces. Because the SPL100 uses a 532 nm laser, which can penetrate water, bathymetric studies using the SPL100 are also possible. Although this will not be examined further, other papers have examined the SPL100 bathymetric performance, e.g., Mandlburger and Jutzi (2019) [18].

Previous research has shown that the SPL100 can be used to measure forest variables such as tree heights and biomass with accuracy similar to linear mode systems [5], [19]. For forest monitoring, the collection efficiency of the SPL is perhaps its most significant advantage over traditional LML. The high point density of the SPL100 and its ability to efficiently map large swaths of forested areas in less time is a more cost-effective way to monitor forest health, logging, fires, and other time-sensitive concerns [5]. While there is a clear interest in vegetation analysis with the SPL100, current studies have focused primarily on ground penetration through trees and the ability to estimate forestry parameters. As of yet, no known studies have presented a quantitative analysis demonstrating the distribution of multiple returns in vegetation for the SPL100, which can shed light on the effective, rather than theoretical, pixel recovery time of the sensor.

1.3 Objective and Contributions

The geospatial community does not yet have a thorough understanding of the performance characteristics of SPL and GML. Non-linear photon detection, using either single photon lidar or Geiger-mode lidar, is not an emerging technology, but applying these techniques for commercial surveying and mapping, however, is new [20]. The primary purpose of this thesis, therefore, is to build towards a more complete

understanding of the geospatial quality of the lidar data produced by the Leica SPL100 airborne single photon system. The research presented in this thesis will examine the data quality and accuracy of the SPL100 point cloud and derived digital elevation models (DEM). The analysis will also compare the current capabilities of the SPL100 to those of conventional LML systems.

There are four primary objectives this thesis seeks to address. Firstly, there will be an evaluation of the horizontal and vertical accuracy of the SPL and LML point clouds on known features using survey-grade GNSS observations. There will also be an examination of SPL and LML point cloud precision using an analysis of flat surfaces of various materials and with different angles of incidence. In addition to these localized quality checks, there will also be a comparison of an SPL100-derived DEM to that of an LML DEM. The final objective is a quantification of precision under tree canopies and the SPL100's ability to resolve multiple returns through vegetation.

2. Lidar Systems

Lidar (Light Detection and Ranging) systems use light, typically in the form of a pulsed laser, to make accurate distance measurements. Lidar systems are thus active sensors, meaning they provide their own energy source to illuminate the target and produce a measurement. In contrast, passive sensors, such as traditional film and digital cameras, record reflected solar electromagnetic radiation. There are two traditional methods to measure long distances with lasers: pulsed and continuous wave systems [1]. Most airborne lidar sensors are pulsed systems, which use short, discrete laser pulses and rely on the precise measurement of the time of flight (TOF). TOF refers to the two-wave travel time from when the pulse is emitted and when it returns to the sensor after reflecting off a target. The range between sensor and target can be solved by

$$d = c\frac{t}{2}, \tag{2-1}$$

where c is the speed of light adjusted for the refractive index of air and t is the total travel time. Alternatively, continuous wave, or phase-based systems, emit a continuous beam of laser radiation and determine distance using the phase difference of the emitted and received signals. Continuous wave systems are not commonly used in airborne surveys, however. A notable exception is the Scanning Laser Altitude and Reflectance Sensor (ScaLARS), operated during the 1990s [21], [22].

Lidar systems can be mounted on a variety of airborne and terrestrial platforms, and are commonly flown on airplanes for mapping studies. Airborne laser scanning (ALS) began in the 1960s and 1970s with profilers that could only record a two-dimensional topographic cross-section along the flight line [1]. Because a laser beam has a narrow instantaneous field of view (IFOV), the beam must be moved across the flight

direction to obtain area coverage instead of a profile [23]. Typically, mechanisms such as rotating mirrors and prisms are used to create a scan pattern on the ground. Improvements in computing, scanning mechanisms, and GPS/IMU (Global Positioning System/ Inertial Measurement Unit) technology in the 1990s began the advent of modern lidar systems, which are capable of collecting three-dimensional distributions of georeferenced points. Current linear mode sensors can produce data at 2–4 points/m^2 at a flying altitude of 2100 m above ground or lower [4]. The USGS Lidar Base Specification v1.3 requires an aggregate nominal pulse spacing of ≥ 8 pulses/m^2 for quality level 1 data, and ≥ 2 for quality level 2 [17]. Additionally, modern lidar systems can achieve centimeter to decimeter absolute vertical accuracy [1]. The USGS specifications state that QL1/2 data must be under ≤ 0.196 m for non-vegetated absolute vertical accuracy [17].

2.1 Multiphoton Detection

The most mature and widely-used lidar technologies are pulsed systems that utilize avalanche photodiodes (APD) operating in linear mode [1], [2]. In its linear mode, an APD generates an electrical signal proportional to incident photon flux (Figure 2). Hence, these systems are referred to as linear systems. Because the sensor has a multiphoton detection threshold, they may also be called a multiphoton lidar (MPL). At a minimum, hundreds of photons are needed to generate a detector response in a linear system. Linear systems use high energy lasers and broad pulse widths of a few nanoseconds to achieve a high signal-to-noise ratio (SNR) [2], [24].

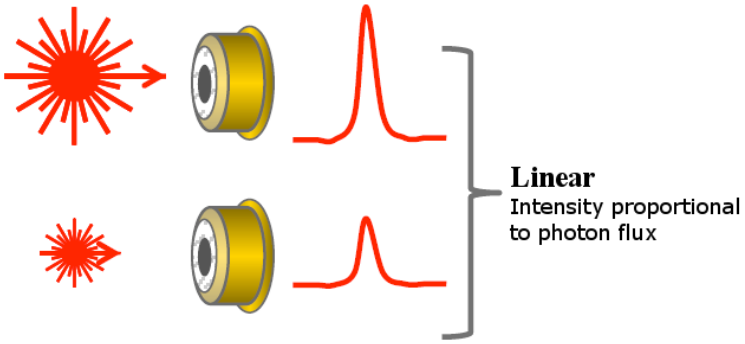

Figure 2: Linear mode APD response[2]

Linear mode systems can provide either discrete returns or digitized waveforms (Figure 3). Ranging for a discrete system is done by estimating the peak, or multiple peaks, of the return energy in hardware, in real time. A constant fraction discriminator (CFD) circuit is generally used as it is invariant to changes in pulse amplitude [1]. The CFD combines the return waveform with a delayed, inverted, and scaled copy of itself [1], [2]. Discrete ranges can be identified from zero-crossing points on the combined signal. Early discrete lidar systems could only record one backscattered echo per emitted laser pulse, with later discrete systems introducing the capability to record multiple returns per pulse [25]. Full-waveform systems, however, return intensity information over the entire observed vertical or horizontal structure by digitizing the entire backscattered echo waveform. In post-processing, improved multi-target resolution along the digitized waveforms is possible through decomposition or deconvolution of the waveform [25], [26]. Because of this, full-waveform lidar is especially useful for

[2] Figure source: Leica Geosystems

vegetation studies. A detailed canopy profile that includes intermediate peaks allows for estimation of characteristics such as biomass [25]. By using a green laser for water penetration, bathymetric lidar surveys can also utilize full-waveform data to understand water column scattering properties and measure water depth [27].

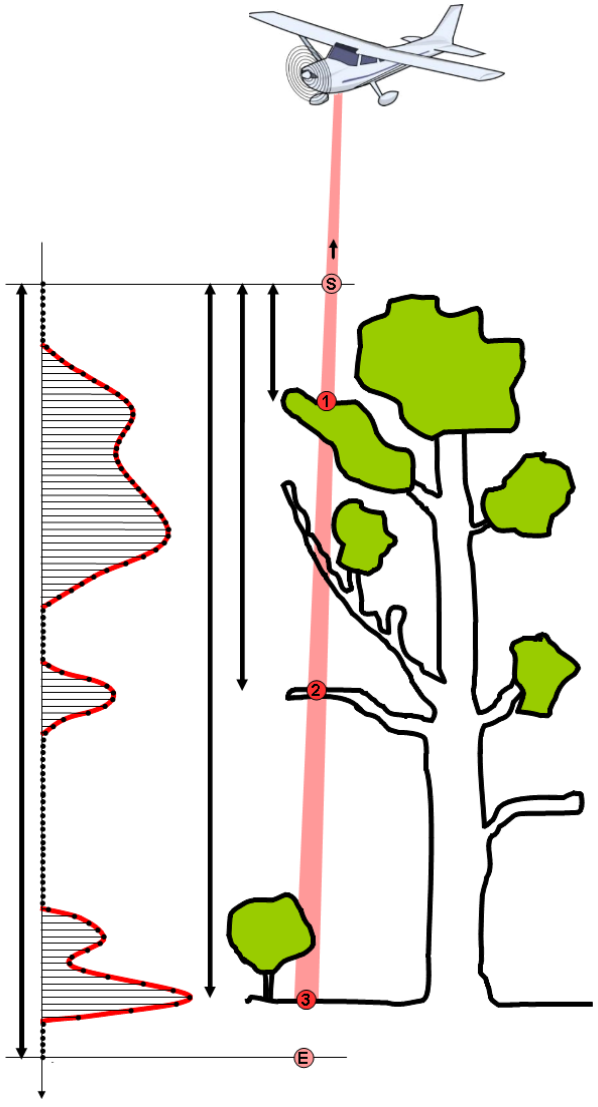

Figure 3: Full-waveform lidar versus discrete return lidar

2.2 Single Photon Detection

It is possible to design lidar detectors that are sensitive to individual photons. Such systems can achieve range measurements with a single photon rather than hundreds or thousands of photons. Lidar systems capable of single photon detection are a new development for the commercial market, and there are currently two competing technologies: single photon lidar (SPL) and Geiger-mode lidar (GML) [3], [4], [13]. The most recent SPL instrument is Leica's SPL100, based on Sigma Space's High-Resolution Quantum Lidar System (HRQLS), while Harris Corporation's IntelliEarth utilizes GML. In contrast to traditional linear (multi-photon) systems, both SPL and GML have an array of detector elements and transmit lower energy laser pulses with shorter pulse widths [2], [4], [24]. Regardless of the sensor design, linear lidar, SPL, and GML are all pulsed systems that calculate range measurements based on TOF.

The primary advantage of SPL and GML is their efficiency; they boast faster acquisition rates than linear systems [3]–[5]. Extremely sensitive detectors allow these systems to fly at higher altitudes, and using an array of detectors ensures high point density even at these altitudes. This efficiency comes at the cost of reduced ranging precision because each range measurement is determined from individual triggering photons [11], [12]. As would be expected, photon-sensitive detectors are highly susceptible to background noise from solar illumination during the daytime as well as detector noise (dark counts) [3]–[5], [24]. The use of narrow bandpass filtering, smaller field of views (FOVs), and noise filtering algorithms can mitigate the effects of solar illumination. Because the output from LML systems is well above the noise level of the detector, single photon solar or dark count events do not affect the data as it does with

SPL. As a final point of consideration, studies on SPL and GML range accuracies have just begun (e.g., Stoker et al., 2016), and further investigation is needed. Linear mode lidar, however, is a mature technology capable of low range noise and high precision [11].

SPL and GML require detectors that are sensitive to individual photons and are capable of determining exact arrival times. Until recently, the two primary choices were photomultiplier tubes (PMTs) and Geiger-mode APDs, but new silicon photomultipliers (SiPMs) present an attractive alternative to both (Figure 4) [28]. Massachusetts Institute of Technology's Lincoln Labs pioneered research into Geiger-mode lidar in the late 1990s, and subsequent private industry and military GML systems include JIGSAW, FOPEN, ALIRT and HALOE [13], [29]. In 2015, Harris Corporation's IntelliEarth became the first commercial Geiger-mode lidar system. Sigma Space's HRQLS relied on microchannel plate photomultiplier tubes, but its successor, the Leica SPL100, uses SiPMs instead.

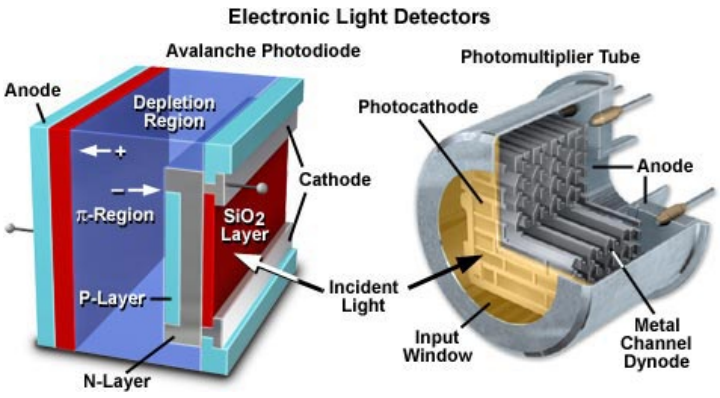

Figure 4: Illustrated examples of photodetectors[3]

[3] Figure source: Hamamatsu http://hamamatsu.magnet.fsu.edu/articles/digitalimagingdetectors.html

2.2.1 Geiger-Mode APDs

An avalanche photodiode internally multiplies photocurrent when a reverse voltage is applied, which enables the measurement of low-level light signals [30]. As previously discussed, the APD response can be highly linear (a detector's linearity refers to the degree the output response is proportional its input) when the reverse voltage is operated below a so-called breakdown voltage (Figure 5) [30]. If the reverse voltage applied is above this breakdown voltage, the APD will operate in its Geiger-mode. Above the breakdown voltage, a single photon can trigger a self-sustaining avalanche current [31]. Regardless of the number of photons received, once triggered the output voltage saturates. Because of this, a Geiger-mode APD (GmAPD) can only provide a binary response, unlike a linear-mode APD (Figure 2, Figure 6). The APD must be reset through a process referred to as "quenching" before another photon can be detected.

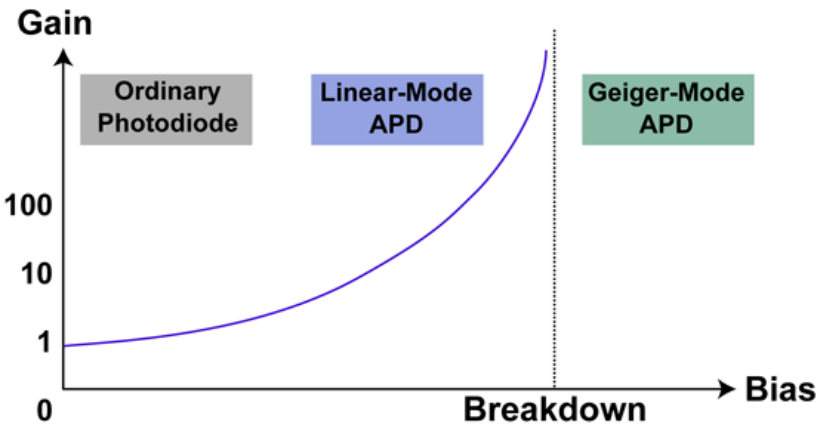

Figure 5: Multiplication (gain) versus reverse bias of avalanche photodiode [4]

[4] Figure source: MIT Lincoln Labs
https://www.ll.mit.edu/mission/electronics/ait/imaging-technology/geiger-mode-photodiodes.html

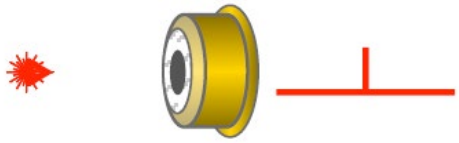

Figure 6: Binary response from a Geiger-mode APD using lower pulse energy[5]

Harris Corporation's IntelliEarth makes use of not a single detector, but an integrated array of thousands of these Geiger-mode APDs (GmAPDs) [13]. The most significant limitation of the IntelliEarth is the relatively long dead time. The detector dead time refers to the time needed for the sensor to reset itself from a detection event so that it is ready to detect another photon; it may also be called recovery time or blanking loss. Current GmAPDs have dead times of around 50 – 1600 ns, meaning objects require a 7.5 m – 240 m separation, respectively, to be distinguished [3]. This dead time constrains IntelliEarth's ability to detect occluded targets, such as penetrating through multiple vegetation layers [4], [11]. Because of the long dead time, each GmAPD detector usually has only one measurement opportunity per imaging cycle [13]. This limitation is compensated for with high PRF and large detector arrays, but future asynchronous readout circuits could enable multiple TOF measurements per imaging cycle. Furthermore, because a GmAPD can only provide a binary response, intensity information is not directly available.

[5] Figure source: Leica Geosystems

2.2.2 Photomultiplier Detectors

In contrast to GML with the IntelliEarth, which utilizes an array of individual GmAPDs, SPL instead uses photomultipliers, such as tubes, microchannel plates, or silicon, which have much shorter dead times [3], [32]. Sigma Space's HRQLS, the precursor to the Leica SPL100, used microchannel plate photomultiplier tubes (MCP-PMTs). Now, the SPL100 uses a silicon photomultiplier (SiPM).

Conventional photomultiplier tubes, which have been available since the 1930s, are extremely sensitive detectors capable of multiplying the current produced by incident light. They consist of a vacuum tube with an input window, a photocathode, focusing electrodes, an electron multiplier (dynodes) and an anode sealed into an evacuated glass tube (Figure 7, Figure 8) [33]. In a process referred to as the external photoelectric effect, the photocathode emits free electrons when light strikes it. These electrons are then accelerated with a high voltage and focused onto the first dynode, where they are multiplied by secondary electron emission. This process is then repeated in successive dynodes. Around the 1980s, microchannel plates began to be incorporated into PMTs in place of the conventional discrete dynodes for photon counting applications (Figure 9) [34], [35]. These microchannel plate photomultiplier tubes (MCP-PMTs) feature a two-dimensional array of channels bundled in parallel in the shape of a disc, where each channel acts an independent electron multiplier [33]. MCP-PMTs are more compact than traditional PMTs, have improved spatial and time resolutions, and have a higher tolerance to magnetic fields [34].

Figure 7: Example of a typical photomultiplier tube

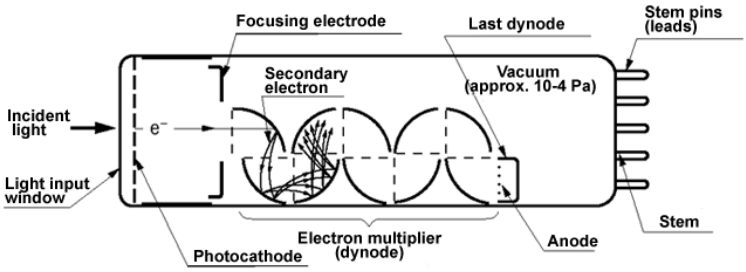

Figure 8: Cross-section of a photomultiplier tube[6]

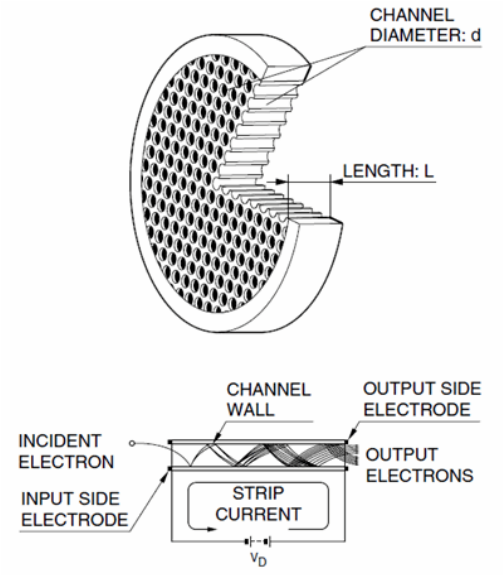

Figure 9: Cross-section of a microchannel plate

[6] Figure source (middle and bottom): Hamamatsu's *Photomultiplier Tube Handbook* [33]

Because photomultiplier tubes are widely available and well-established, they have been an attractive option for single photon counting. There are, however, several significant drawbacks to using PMTs, particularly their mechanical complexity and sensitivity to magnetic fields [31]. Additionally, currently available photon-counting PMTs' have peak sensitivities in the visible wavelengths, which limited the HRQLS system to operating at 532 nm (Figure 10) [3]. The advantages of solid-state silicon detectors like the SiPM include increased compactness, mechanical robustness, higher quantum efficiency, lower operation voltages and insensitivity to magnetic fields [31], [36], [37].

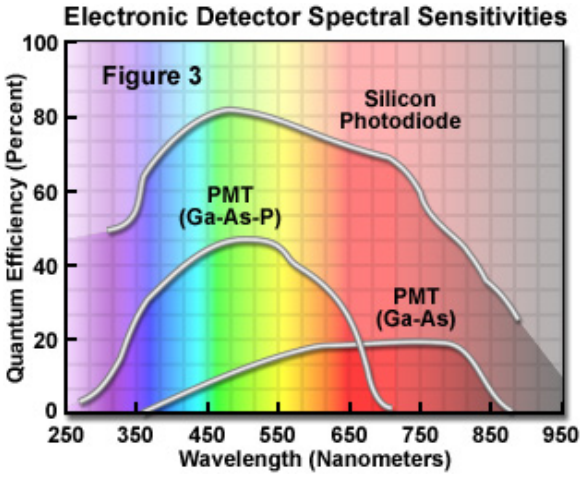

Figure 10: Spectral sensitivities of photodetectors[7]

Because of these advantages, silicon photomultipliers (SiPM), which have been available since the 2000s, are now a viable alternative to PMTs, MCP-PMTS, and APDs for photon counting applications such as SPL [28], [38], [39]. A SiPM consists of an

[7] Figure source: Hamamatsu http://hamamatsu.magnet.fsu.edu/articles/digitalimagingdetectors.html

array of densely packed (1000–5000 per mm^2) Geiger-mode APDs arranged on a single chip, each with their own quenching resistor and connected in parallel to a single output [31]. A microcell on this array is comprised of an independent Geiger-mode APD and its quenching resistor. Each microcell in the array detects and amplifies the charge from incoming photons, but are decoupled from each other so that the final detector output is the sum of the number of microcells triggered [30], [31]. The Leica SPL100 system features a 10 x 10 matrix of detector cells, each of which consists of many closely-spaced GmAPD microcells (Figure 11). The detector cell array is roughly analogous to pixels, but it is essential to bear in mind that the SiPM is not an imaging device.

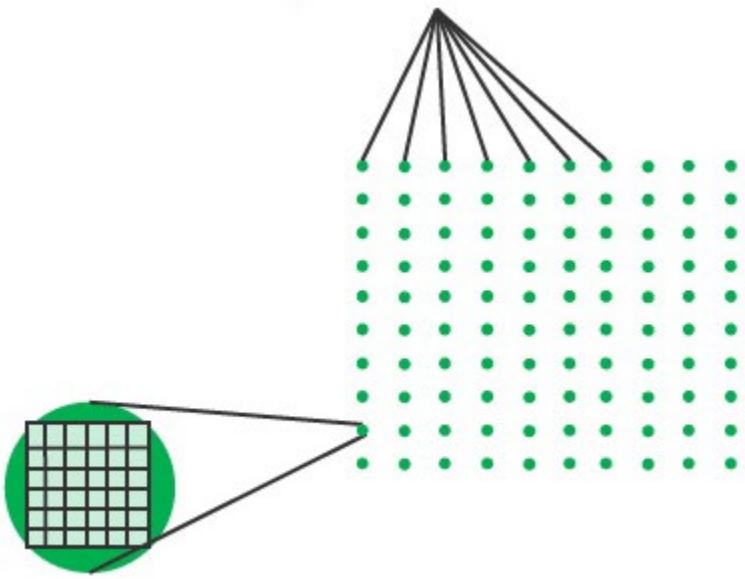

Figure 11: Illustration depicting the structure of the SPL100 detector and microcells (from Mandlburger et al. 2019)

Using SiPMs overcomes some of the limitations of quenching recovery times and the lack of proportionality to the incident flux inherent to using a single detector, as described in section 2.2.1 [31], [36], [37]. The system's dynamic range is determined by the total number of microcells and the microcell recovery time [30]. If the number of photons received is much less than the number of microcells, the signal is relatively linear. Because of this, SiPM linearity gets worse as the number of incident photons increases; the output saturates when the number of photons is about equal to the number of microcells [30], [31]. The biggest downside to SiPMs is the high dark count rate, which results in increased noise as compared to using MCP-PMTs [37]. Other limitations include optical crosstalk and limited sensor area [40].

2.3 Leica SPL100

2.3.1 System Design

The Leica SPL100 system achieves a high density of returned points (12-30 points per sq. meter) by splitting the outgoing laser beam using a diffractive optical element to create a 10 x 10 array of "beamlets," which are then captured by a 10 x 10 SiPM array. A rotating prism, referred to as an optical wedge, is used to generate a circular scan pattern on the ground [41]. In the SPL100, each of the 10 x 10 cells consists of closely-spaced GmAPD microcells, allowing multiple photons to be detected by each cell [15], [32]. Because of this, the SPL100 can deliver a rough estimate of intensity, an uncalibrated measure of the strength of the returning laser pulse. Intensity is typically recorded as the peak amplitude in an LML system, but in the SPL100, the intensity is the pulse width derived from the distance between the recorded rising and falling edges. A summary of

system properties for linear mode, Geiger-mode, and single photon lidar systems is presented in Table 1. The table has been adapted from Jutzi (2017) and updated with information from the Leica SPL100 product specification sheet [6], [14], [42].

Table 1: Typical system specifications for LML, GML, and SPL (Jutzi 2017)

Type	Linear Mode Lidar (LML)	Geiger Mode Lidar (GML)	Single Photon Lidar (SPL)
Technology	Various companies	Harris IntelliEarth	Leica SPL100
Laser Wavelength	532/1064/1550 nm	1064 nm	532 nm
Laser Pulse Width @ FWHM	1-5 ns	0.55 ns	0.6 ns
Laser Beam Divergence @ $1/e^2$	0.25-1 mrad	~ 5 mrad	0.08 mrad/beamlet
Field-of-View (FOV)	≤ 72°	30°	20°, 30°, 40° or 60° fixed
Detector Elements	1-2 PIN/APD	128x32 = 4096 GmAPD	10x10 = 100 PMT/SiPM
Min. Surface Detection	250-10000 Photons	8 – 10 Photons	1 Photon
Instantaneous FOV (IFOV)	0.25-1 mrad	0.035 mrad	0.13 mrad
Jitter Timing (Precision)	50 – 500 ps	250 – 500 ps	50 – 100 ps
Blanking Loss/Dead/Recovery Time	N/A	50-1600 ns typical	1.6 ns
Pulse Repetition Frequency (PRF)	≤ 2000 kHz	50-60 kHz	60 kHz
Max. Flying Height (AGL)	≤ 5000 m	≤ 11000 m	≤ 4500 m
Aerial Coverage @ 8 pts/m^2	≤ 450 km^2/h	≤ 2000 km^2/h	≤ 1000 km^2/h

2.3.2 Ranging Noise

The fundamental measurement of a lidar system is the distance, or ranging, measurement. Ranging noise, or ranging precision, describes the repeatability of the lidar measurements, i.e., random error. A GmAPD will produce lower ranging precision as compared to LML [11], [12]. To see why this is, consider that the received pulse, h_r, is a temporal convolution of the instrument response function, h_{IRF}, and the surface response function, h_{SRF}, expressed as

$$h_r(t) = h_{IRF}(t) * h_{SRF}(t) . \tag{2-2}$$

The received echo pulse thus has a width and shape that is dependent on the properties of the target surfaces it interacted with (reflectivity, roughness, slope, etc.) and the parameters of the sensor (pulse width, pulse power, etc.) [26], [43]. When acquiring data with a GmAPD, each photon that is detected originates from somewhere in this distribution, and because of this, there is a significant range uncertainty. If the device took enough samples of the same footprint, the histogram of time-of-flights recorded from each photon detection event would eventually reconstruct the temporal waveform of the return pulse, equivalent to the digitized waveform captured by full-waveform lidar [14]. For an analog lidar device (LML), many photons are detected at once, generating the same waveform distribution but per laser shot. Ranging is done by estimating the peak, or multiple peaks, of the return energy either in hardware or by digitizing the entire backscattered echo waveform [1], [15]. The accuracy and precision of range estimation are proportional to the signal-to-noise ratio and the inverse of the pulse width [2], [12].

It is also expected that surface roughness or steepness will significantly worsen the ranging precision in an SPL system. Adding slope or roughness to the target surface will broaden the convolved temporal shape of the received pulse, creating further distribution uncertainty in single photon detection [43]. This effect is also seen in LML but is not as pronounced because although the pulse widens, using peak detection for ranging results in less uncertainty. Although studies on SPL100 performance are limited, research from Mandlburger et al. (2019) supports this theoretical basis, finding a 9.8 cm dispersion for tilted roofs as compared to 1.2 cm for flat roofs and 1.5 cm dispersion for paved surfaces as compared to 5.8 cm for meadows (increased roughness). Another study by Yang et al. used a Monte Carlo simulation to show that atmospheric conditions and surface roughness will increase uncertainty in the ICE-Sat2, a space-borne SPL [44].

2.3.3 Additional Error Sources

The previous section addressed the intrinsic ranging precision of the SPL100 system, but other error sources will contribute to the uncertainty in the final data product. The errors associated with the georeferencing subsystems are particularly important to consider. Without knowing the precise position and orientation of an airborne lidar system throughout the flight, the range measurements collected would be meaningless. To this end, three primary subsystems are used to collect data: a Global Positioning System (GPS) for location, an Inertial Measurement Unit (IMU) for orientation, and the laser scanner assembly [1]. The raw navigation records (GPS/IMU) are continuously recorded in-flight and must be synchronized with the range measurements post-flight. All of these subsystems contribute to overall error, and the uncertainty in the final point

cloud reflects the combined uncertainties from all the subsystems [45]. Uncertainty analysis for lidar data is non-trivial, as the navigation and ranging measurements are captured in different relative frames of reference and contribute to the overall uncertainty in a non-linear manner [45]–[48]. In addition to the individual errors from the various subsystems, any error in the calibration of the relationship between subsystems will be reflected in the final product.

Information from the GPS and IMU are integrated in post-processing to georeference the data. The origin of each of these subsystems are not co-located, however, and therefore they each have different frames of reference. The process of transforming the data amongst the different coordinate systems to calculate ground coordinates can be expressed through the following georeferencing formula [1], [45]:

$$\mathrm{P}_G^m = \mathrm{P}_{\mathrm{GPS}}^{\mathrm{m}} + \mathrm{R}_{\mathrm{b}}^{\mathrm{m}}\left(\mathrm{R}_{\mathrm{s}}^{\mathrm{b}} \cdot \mathrm{r}^{\mathrm{s}} - \ell^{\mathrm{b}}\right), \tag{2-3}$$

where:

P_G^m: Coordinates of the target point in the mapping frame (m)

$\mathrm{P}_{\mathrm{GPS}}^{\mathrm{m}}$: Coordinates of navigation sensor (GPS) in mapping frame (m)

$\mathrm{R}_{\mathrm{b}}^{\mathrm{m}}$: Rotation matrix from body frame (b) to the mapping frame (m)

$\mathrm{R}_{\mathrm{s}}^{\mathrm{b}}$: Rotation matrix from laser scanner frame (s) into the body frame (b) (Usually referred to as boresight matrix)

r^{s}: Coordinates of the target point in laser scanner frame (s)

ℓ^{b}: Lever arm from scanner origin to navigation center origin given in the body frame (b)

The georeferencing formula can alternatively be expressed more completely as

$$\begin{bmatrix} X \\ Y \\ Z \end{bmatrix}_G^m = \begin{bmatrix} x \\ y \\ z \end{bmatrix}_{GPS}^m + \mathrm{R}_{\mathrm{b}}^{\mathrm{m}}(\omega, \varphi, \kappa) \cdot \left(\mathrm{R}_{\mathrm{s}}^{\mathrm{b}}(\mathrm{d}\omega, \mathrm{d}\varphi, \mathrm{d}\kappa) \cdot \mathrm{r}^{\mathrm{s}}(\alpha, d) - \begin{bmatrix} \ell_x \\ \ell_y \\ \ell_z \end{bmatrix}^{\mathrm{b}} \right). \quad (2\text{-}4)$$

The GPS (x, y, z), IMU (ω, φ, κ), scanning mirror unit (α), laser ranging unit (d) and component integration all contribute to the overall error [45]–[48]. The system integration includes the boresight angles (dω, dφ, dκ), and lever arm offset (l_x, l_y, l_z). Thus, the basic characterization of lidar error includes 14 parameters [45], [48]. A georeferenced point cloud contains random error that occurs as a result of unpredictable sampling variability as well as possible systematic biases that can arise from system imperfections or human errors such as incorrect calibration. Although the above georeferencing equations apply to any lidar system, there are concerns specific to the SPL100 to note. Because the SPL100 is designed to be flown at higher altitudes (~2,000-4,500 m) than traditional LML, this will result in larger uncertainty in the IMU output because angular error increases proportionally with object distance [45], [47]. Angular biases, atmospheric refraction, and pulse group velocity effects also have a more significant impact on geolocation accuracy due to the longer slant range distances, but Sigma Space has applied algorithms to account for these problems [3].

Imperfections in the rotating prism wedge, which produces the circular scan pattern on the ground, also exist in the SPL100. A slight wobble in the vertical axis in which the prism spins can produce small pointing errors whose influence will be magnified on the ground due to the higher altitudes the SPL100 operates at [41]. Pan et al. (2017), demonstrated how each HRQLS system has a unique wedge calibration which needs to

be reassessed whenever new boresight angles are required. Uncertainty in the final point cloud may also be introduced from misalignments of the returned laser array on the detector array. The images of the beamlet array may become displaced relative to their assigned pixel centers due to long pulse TOFs and high scan speeds [3], [7]. By the time the receiver views the photons returning from the surface, the optical wedge has advanced in phase relative to the time of laser fire [49]. Thus, the receiver FOV is displaced from the area of illumination on the ground. The HRQLS and the SPL100 systems address this by implementing an optical TOF correction using an annular corrector wedge that is attached to the main scanner wedge in order to bring the transmitter and receiver FOVs into alignment for a specific flying height (Figure 12) [3], [7], [49]. Although the angular speed of the scanner can be adjusted for different flying heights to maintain alignment, high terrain relief or significant altitude changes during flight may result in the corrector wedge being insufficient to compensate for the movement [3], [50]. The SPL100, therefore, uses receiver-based georeferencing, where the timing and pointing are tied to the detector pixels rather than the "laser-centric" model traditionally used in LML sensors [50]. In the laser-centric model, the direction of the outgoing laser beam is used for determining point position on the ground. Taken together, any errors in this process would result in the beamlets striking the wrong detector element. As of yet, no studies have examined how possible misalignments impact the total expected error budget.

Additional accuracy issues may arise for an SPL system in the form of systematic ranging biases that occur due to an effect referred to as "first photon bias." Because photon arrival times follow a Poisson distribution and photon-sensitive detectors only

record the arrival time of the earliest photon, the range to the target appears to be closer to the sensor [11], [43]. The bias is affected by the number of incoming photons, and less incoming photons will make the target appear farther away [43], [44]. Such systematic ranging biases can be partly compensated for if the signal strength is known, but no specific information has been made available regarding the SPL100's handling of the first photon bias.

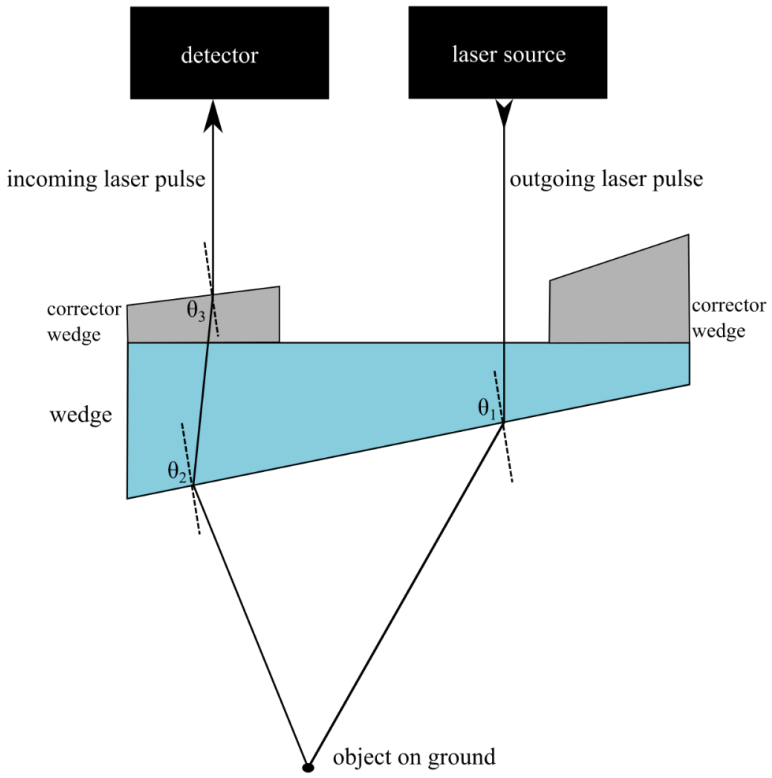

Figure 12: Side profile of spinning prism wedge and corrector wedge

3. Data Sources

Single photon lidar (SPL) and linear mode lidar (LML) data were collected over the University of Houston campus (Houston, TX, USA) in February 2017 using the SPL100 and Optech Titan systems, respectively. The Optech Titan is a discrete return system with three independent wavelength channels at 1550, 1064, and 532 nm [51]. Later, in November 2018, a GNSS survey of the campus was conducted. This chapter will detail these collections and the processing procedures applied to them.

3.1 Airborne Lidar Data Collection

The SPL100 was flown over Houston by Leica on February 25, 2017, during leaf-on conditions and was operated at 12,000 ft. (~3700 m) above ground level (AGL). The SPL data was provided in the WGS84(G1762) datum. The raw point cloud from the SPL100 is intrinsically noisy due to false returns from solar illumination and dark counts. Because of this, noise filtering is an essential step in post-processing single photon and Geiger-mode data. The SPL100 data was post-processed and noise filtered using the proprietary algorithms in the Leica HxMap software. The data was initially processed in 2017 and reprocessed in 2019 with an updated version of the HxMap software. In both cases, the processing was performed by, or under the direct guidance of, Leica employees. The Optech Titan was flown over the University of Houston campus on February 16, 2017, at 1640 ft. (~500 m) AGL by the National Center for Airborne Laser Mapping (NCALM). NCALM also performed data processing using Optech LMS and TerraScan and made the data available in NAD83(2011) with NAVD88 orthometric

heights. Intensities were normalized to a flying height of 1000 m. The survey boundaries of these two missions are shown in Figure 13.

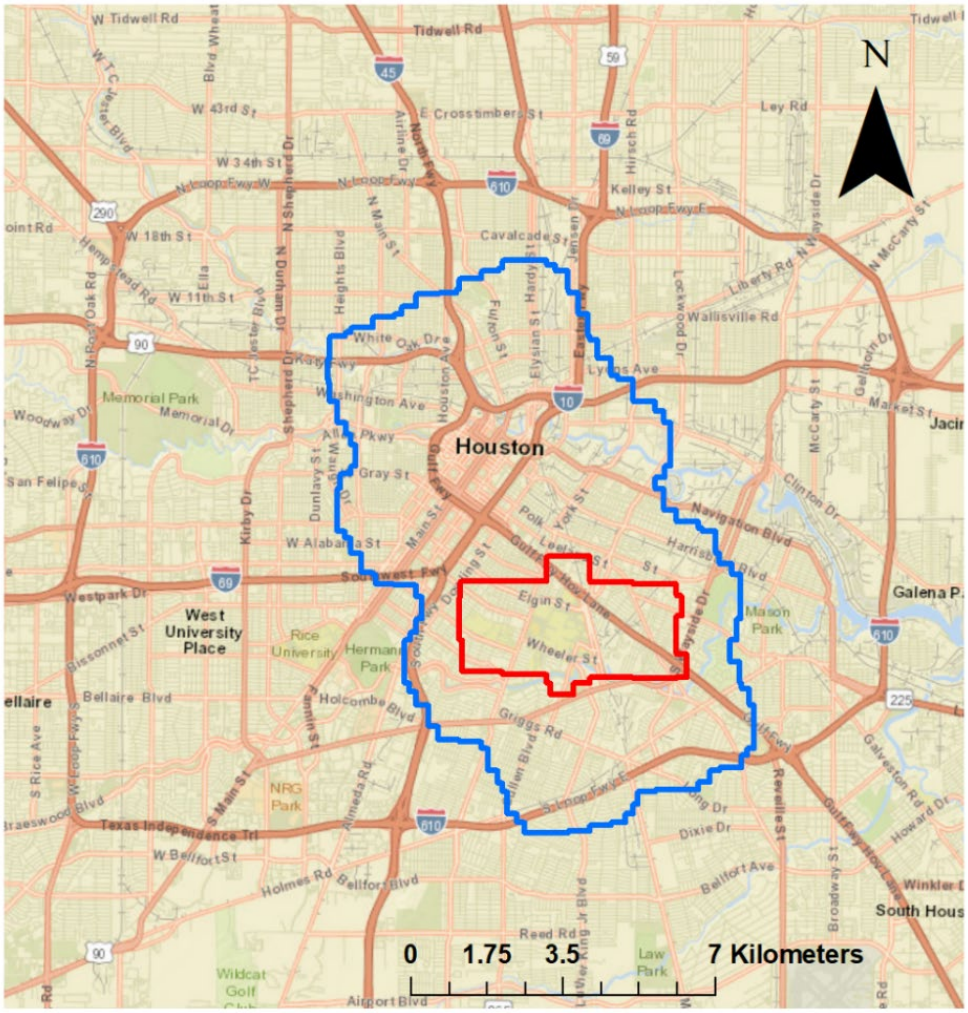

Figure 13: Survey boundaries of the LML and SPL datasets

Table 2: Summary of Flight Parameters

	SPL100	Optech Titan
Flying Height	12,000 ft (~3700 m)	1640 ft (~500 m)
Laser Wavelength	532 nm (visible)	1550 nm (IR) 1064 nm (NIR) 532 nm (visible)
Pulse Repetition Frequency	50 kHz	175 kHz / channel
Point Density	~25 p/m^2	~12 p/m^2
Expected Vertical Precision	< 10 cm*	< 2 cm**

* Mandlburger et al. (2019)
** Fernandez-Diaz et al. (2016)

3.2 GNSS Data Collection

Global Navigation Satellite System (GNSS) data were collected throughout the University of Houston survey area in November 2018. Because this survey was conducted long after the lidar collections, each site was carefully chosen to ensure it could be clearly distinguished in the SPL and LML point clouds and that its location had not changed. Candidate sites had flat surfaces and sharp, distinct corners (e.g., raised flower beds, benches, concrete blocks). In the field, a rapid static survey was performed at thirty-four different sites using a Trimble NetR9 GNSS receiver (Figure 14, Figure 15). Rapid static surveys can produce centimeter-level accuracy with short observation times of 5-30 minutes [52]. For this study, all sites were observed for at least 40 minutes.

Figure 14: Examples of GNSS survey locations

The GNSS data were post-processed using the National Geodetic Survey's Online Positioning User Service (OPUS)[8] website, as well as the software package GrafNet, which was used to post-process data for days in which OPUS produced poor results. OPUS allows users to upload GPS data freely and returns an email report containing the positional coordinates and other quality information. OPUS has two different processing algorithms depending on the length of the data observation: OPUS-S for static data between 2-48 hours, and OPUS-RS for rapid static data between 15 minutes and 2 hours. OPUS-RS was used to process the data collected for this survey. Under normal conditions, OPUS-RS can produce centimeter-level accuracy [53].

Both OPUS-S and OPUS-RS algorithms use data from Continually Operating Reference Stations (CORS) within the United States to calculate positional coordinates. The OPUS-RS algorithm, which is optimized for short observation times, achieves high accuracy by using three to nine CORS to estimate atmospheric delays at the rover (surveyed site) [54]. Estimates of the rover's coordinates are calculated using data from each of the selected CORS individually; then the final coordinates are computed with a simultaneous least-squares adjustment of all the data together [53], [55]. In the OPUS-RS email report, users are given an estimated uncertainty for each component of the final positional coordinate. A root-mean-squared difference (RMSD) for each component is calculated from differences between the final coordinate and the coordinates calculated using only individual CORS data [53], [55]. These error estimates can help determine if the survey quality is within the required tolerance. It is suggested that for a high-quality

[8] OPUS: http://geodesy.noaa.gov/OPUS/

survey, the RMS difference in latitude, longitude, and ellipsoidal height should be less than 5 cm [56]. OPUS-RS also provides two “quality indicators” related to estimating atmospheric parameters and the rover position. Both should be above three [53], [56]. Given these criteria, positional coordinates with more than 5 cm of horizontal or vertical error, quality indicators less than 3, or those that used less than 50% of total observations were instead post-processed with GrafNet. The final results from the GNSS data collection are included in the Appendix (Table 8, Table 9).

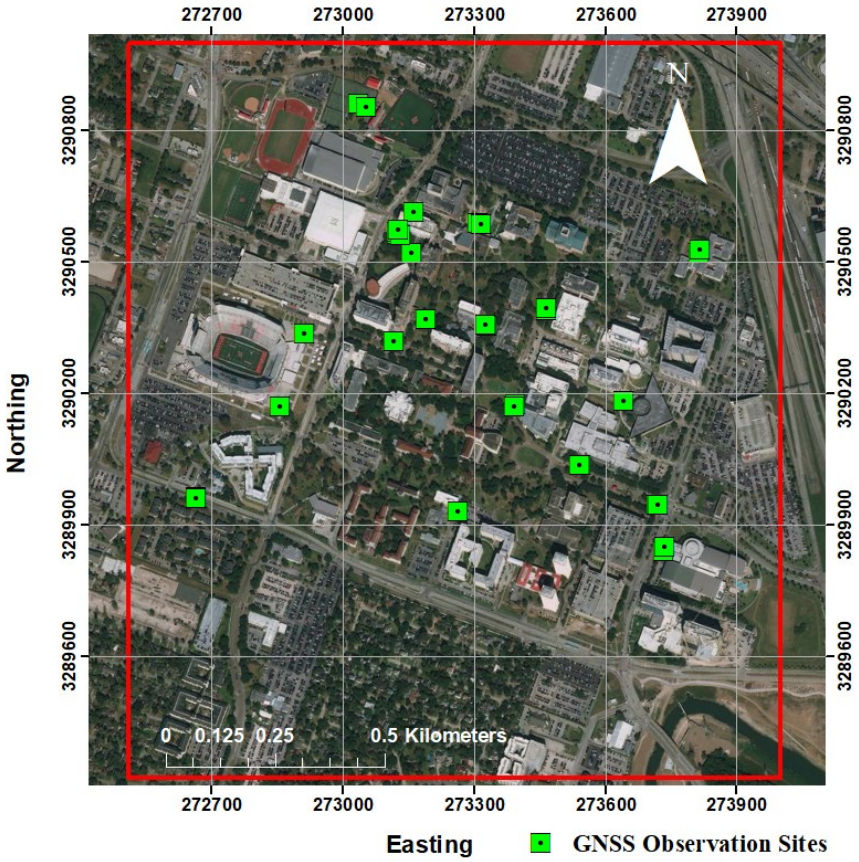

Figure 15: University of Houston survey area and GNSS observation sites

4. Methodology

4.1 Positional Accuracy

The SPL100 data was transformed to the same horizontal and vertical datums as the Optech Titan collection using NOAA's free software VDatum[9]. The SPL horizontal UTM coordinates were shifted from WGS84(G1762) to NAD83(2011), and the elevations were transformed from WGS84(G1762) ellipsoid elevations to NAVD88 orthometric elevations (based on Geoid12B). After this, the areas of interest (the GPS collection sites) were extracted from the full point clouds and then displayed in Matlab to manually determine the point cloud position corresponding to each GPS site. The differences in the horizontal and vertical positions were recorded for every survey location for both the SPL and LML data sets.

4.2 Positional Precision

The TerraScan software package within MicroStation was used to identify and export fifty planar regions throughout the survey site; samples were saved as LAS files to preserve relevant metadata (intensity, flight line, GPS time stamp). These planar regions, which were at least 10 m^2 in surface area, were chosen to include a variety of surface materials and slopes. Many of these samples came from various rooftops of commercial and residential homes, but other flat regions such as sidewalks, tennis courts, and parking lots were also used. The same sample regions were used to analyze both the SPL and

[9] VDatum: https://vdatum.noaa.gov/

LML data sets. The precision of a lidar system can be inferred from measuring the dispersion of elevation values on flat surfaces within a single flight line [57].

Matlab was used to determine both the normal vector of the best-fit plane and the standard deviation of the planar fit for each of the samples (Figure 16). It is important to note that for each sample only points from a single flight line were used, thus removing the possible effects of misalignments between flight lines. Additionally, because the Optech Titan has three lasers at different wavelengths, each of these channels was analyzed separately. After this, the trajectory data was used in conjunction with the best-fit plane to find the angle of incidence of the laser on the sample surface. For each plane, the position of the first time-stamped point was used to construct a laser path vector. The angle of incidence is then simply the angle between the planar normal and laser vector. The mean intensity for each planar sample was also calculated.

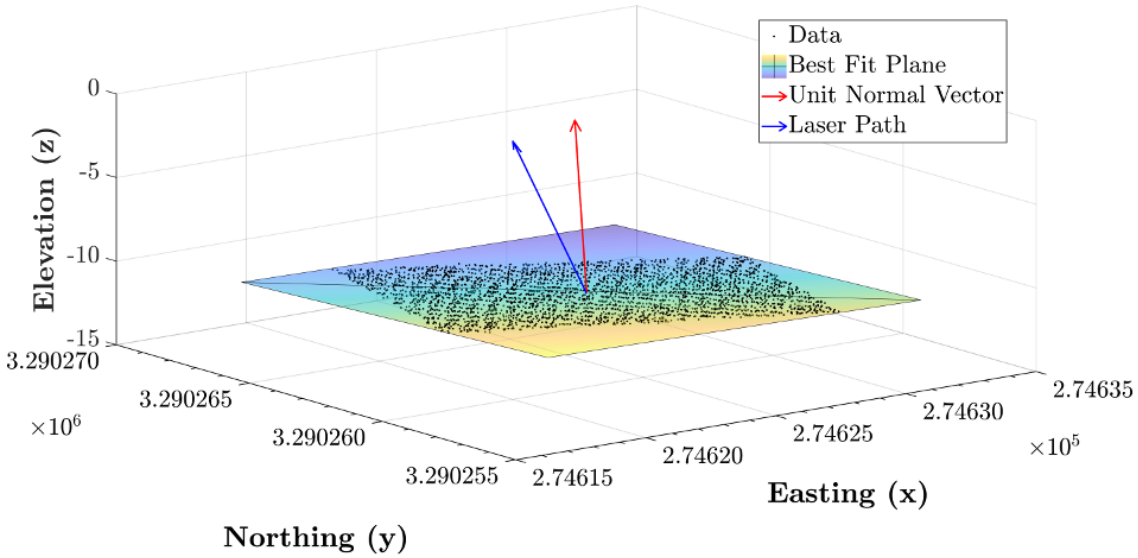

Figure 16: Using planar fitting to find the angle of incidence on a flat sample of points

4.3 DEM Comparison

Before a Digital Elevation Model (DEM) can be generated, lidar returns from the ground must first be identified. This classification was performed using the TerraScan embedded ground classification routine with the default parameters (88° for terrain angle, 10° for iteration angle, and 1.4 m for iteration distance). TerraScan's ground classification routine is based on work by Axelsson (2000) [58]. Before analysis, the SPL dataset was transformed to the same datum as the LML data, as described in Section 4.1. Additionally, the mean elevation bias was subtracted from each data set. (The elevation bias is the mean value calculated from the differences between each GPS survey height and the height of the corresponding point cloud return.) TerraScan provides a simple method for adding a constant Z value to all points with the "Transform Points" tool.

After this, the entire process of generating and comparing DEMs was done with Esri's ArcMap software. In ArcMap, a LAS dataset can be created to reference multiple LAS files and their statistics. The dataset can be configured to filter only points classified as ground returns and to ignore importing other classes. ArcMap can then create a DEM from the elevation values with the "LAS Dataset to Raster" tool. A one-meter resolution image was created for both the LML and SPL datasets using the default parameters (cell assignment based on average value and void filling with linear interpolation). Each DEM raster image was then clipped to a specific spatial extent in ArcMap to ensure matching boundaries before the LML image was subtracted from the SPL using Raster Calculator tools. Some artifacts are visible in this difference of DEM image due to slight differences produced from the ground classification routine in areas with buildings. In particular,

edges of buildings had stray misclassifications, which led to discrepancies between the SPL and LML data.

4.4 Canopy Performance

TerraScan was used to identify areas where the tree canopy completely covered the ground. Those trees were then segmented out and exported to LAS files that could be further analyzed and plotted in Matlab. An important part of this analysis was determining how many of the emitted pulses reached the ground. To accomplish this, Zhang et al.'s cloth simulation filtering (CSF) algorithm (2016) was used to classify ground points [59]. The CSF algorithm creates a surface model by inverting the point cloud and simulating a cloth draped over the terrain (Figure 17). It has been made available in a variety of programming languages, including Python and Matlab, as well as a plugin for the open-source program CloudCompare[10]. The CSF algorithm was more effective at creating a suitable classification for these small sample areas than using TerraScan. The following CSF parameters were used: 0.1 for cloth resolution, 500 iterations maximum, and 0.1 classification threshold.

[10] https://www.mathworks.com/matlabcentral/fileexchange/58139-csf-cloth-simulation-filter
https://github.com/jianboqi/CSF

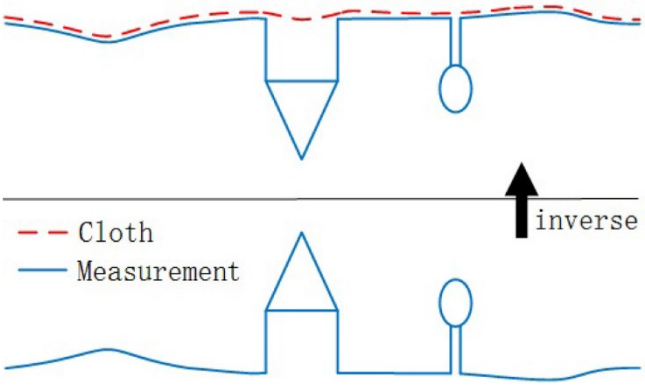

Figure 17: Overview of Cloth Simulation Filtering (Zhang et al., 2016)

A Matlab script was constructed that first identified the number of ground points using the CSF algorithm. After that, all the point cloud returns were sorted by their time stamp. For the SPL100, the returns were further sorted by their beamlet number (1-100), which is stored in the 8-bit "user data" field of the LAS file[11]. Because the LML data was collected with a system with three laser wavelengths, these returns were further sorted instead by the "scanner channel" data field. After thusly organizing the data, it was possible to determine how many emitted pulses were contained within each sample area, distinguishing pulses from different beamlets or channels as appropriate. The LAS file structure also contains data fields that identify, for every point, what return number the point was, and how many total returns the originating pulse contained. This information was used to plot the data by return number and to calculate the vertical separation between multiple returns from the same pulse. The script also found the number of pulses with multiple returns, and how many pulses within the sample area had only a single return.

[11] https://rapidlasso.com/2018/09/14/scrutinizing-lidar-data-from-leicas-single-photon-scanner-spl100-aka-spl99/
https://www.asprs.org/divisions-committees/lidar-division/laser-las-file-format-exchange-activities

5. Results

5.1 Positional Accuracy

The positional accuracy of a lidar system refers to how close a georeferenced position in the final point cloud is to its true, observed location position. Accuracy was assessed by examining the mean vertical and horizontal differences between 33 GNSS collection sites and their corresponding LML and SPL point cloud positions (see Table 3, Table 4). A Z-test was used to determine if the mean differences in easting, northing, and ellipsoidal height were statistically different from zero at a 95% confidence level [60], [61]. The mean easting difference of the Optech Titan data from the GNSS was not statistically significant, nor were the mean easting and northing differences of the SPL100 data. For the remaining values presented in Table 3 and Table 4, the null hypotheses that the mean differences were equal to zero were rejected. With one exception, the horizontal differences are statistically equal to zero, but the vertical differences are not. These mean vertical differences indicate a systematic vertical bias in the point clouds, potentially from the kinematic trajectory solution. This observation fits with the knowledge that the vertical component of a GNSS position is weaker than the horizontal components.

A two-sample Z-test was then used to determine if the mean positional differences for the Optech Titan and SPL100 were statistically different from each other at a 95% confidence level. Although the mean easting differences were not statistically significant, the null hypotheses that the mean differences were equal were rejected for the northing and ellipsoidal heights. The SPL100 data set has a positive elevation bias (11.67 cm)

between the recorded GNSS and point cloud heights, while the Optech Titan has a negative height bias (-13.27 cm). As previously mentioned, these differences from zero are statistically significant at 95% confidence and are therefore clearly statistically different from each other. However, if the vertical biases are examined in terms of their magnitude only, there is no statistical difference in their magnitudes at 95% confidence according to a two-sample Z-test. This result indicates that the vertical accuracy of the SPL100 is similar to the linear mode system despite the worse intrinsic ranging precision. Table 3 and Table 4 also show that the horizontal differences in the Optech Titan had higher standard deviations than the SPL100, which can be attributed to the lower point density of the Optech Titan. By virtue of having denser coverage, the SPL100 is more likely to produce a return that closely corresponds to the corner being measured.

Overall, these results indicate that the SPL100 is capable of similar positional accuracy as a linear mode lidar system, represented here by the Optech Titan, in regards to the final post-processed data product. An important caveat, however, is that the survey sites chosen here consisted of primarily flat, smooth surfaces. In light of the results presented by Mandlburger et al. (2019) and in the next section of this thesis, these error estimates may be optimistic [18]. Over rough terrain or sloped surfaces, SPL100 positional accuracy may be considerably worse than that from a traditional LML sensor.

Table 3: Optech Titan Absolute Horizontal and Vertical Georeferencing Quality

	Δ Easting GNSS	Δ Northing GNSS	Δ Ellipsoidal GNSS
Mean	0.45 cm	12.58 cm	-13.27 cm
Standard Dev	17.83 cm	15.60 cm	7.63 cm
RMSE	17.30 cm	19.56 cm	15.02 cm

Table 4: SPL100 Absolute Horizontal and Vertical Georeferencing Quality

	Δ Easting GNSS	Δ Northing GNSS	Δ Ellipsoidal GNSS
Mean	-2.92 cm	-1.27 cm	11.67 cm
Standard Dev	11.00 cm	10.68 cm	7.88 cm
RMSE	11.05 cm	10.44 cm	13.80 cm

5.2 Positional Precision

As expected, the standard deviation of flat regions is higher in the SPL100 dataset than the linear mode lidar captured with the Optech Titan. The overall standard deviation, calculated from all residuals across the fifty chosen samples, was 3.2 cm for the SPL100. In the Optech Titan, however, it was less than half of that, approximately 1.2 cm (Table 5). When standard deviations were calculated for each sample, the SPL100 also had a much broader range of standard deviations- from 1 cm up to 11 cm. The sample standard deviations for the Optech Titan ranged from a minimum of 0.5 cm to around 3 cm. A two-sample F-test was conducted for each sample to determine whether the differences in planar variances in the SPL and LML data were statistically significant at 95%. Three of the samples from the Optech Titan channel had distributions similar to the SPL100, with the remaining samples showing statistically significant differences in variance, and hence precision. Two of these samples were from the SPL surfaces with the lowest standard

deviations, likely due to bright intensity values and moderate angles of incidence (15° - 20°). The other was from an exceptionally noisy LML sample with an angle of incidence around 30°, whereas the SPL was recorded from an angle of about 11°. Several example surface profiles are shown in Figure 18-Figure 20 (data is shown for a single flight line and with all three Optech Titan channels).

Table 5: Standard Deviation of Planar Surfaces

System	Standard Deviations (cm)
Optech Titan (1550 nm)	1.2
Optech Titan (1064 nm)	1.2
Optech Titan (532 nm)	1.1
SPL100 (532 nm)	3.2

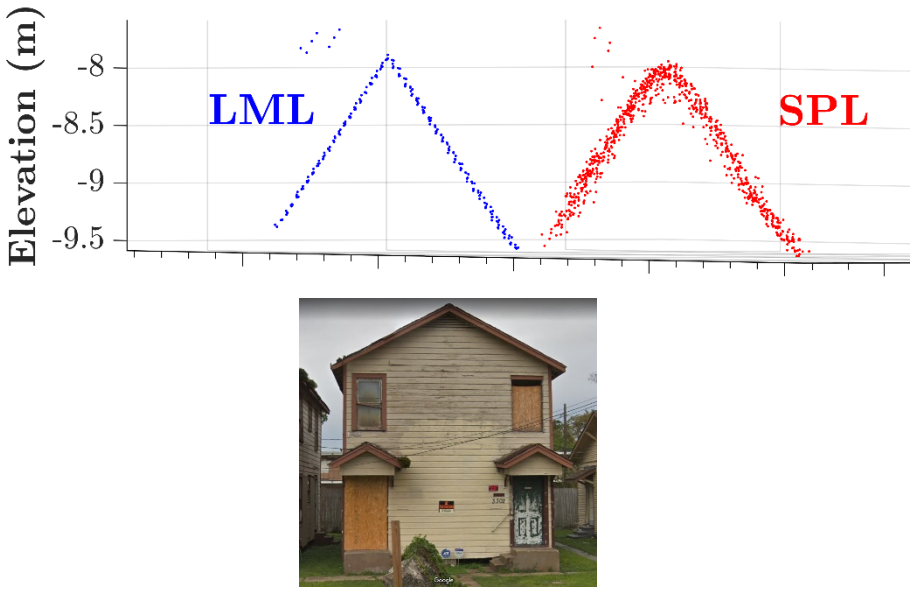

Figure 18: Profile of a sampled roof (~7.5 m wide, σ ~ 1 cm for LML, σ ~ 4 cm for SPL)

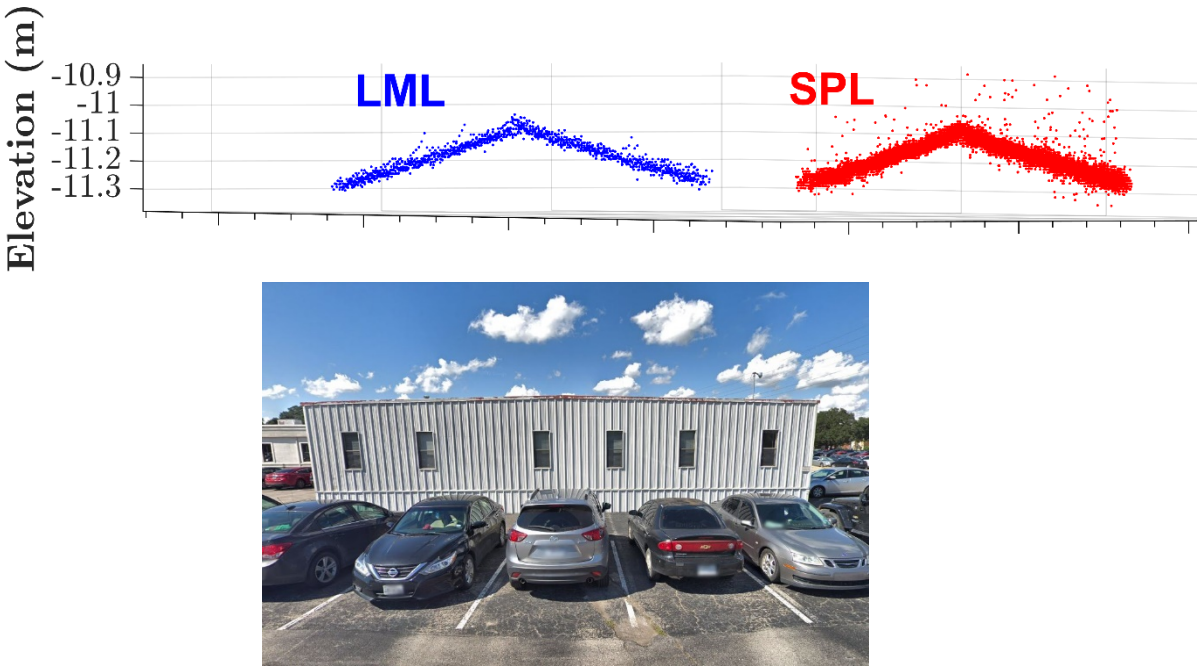

Figure 19: Profile of a sampled roof (~21 m wide, σ ~ 1.6 cm for LML, σ ~ 8 cm for SPL)

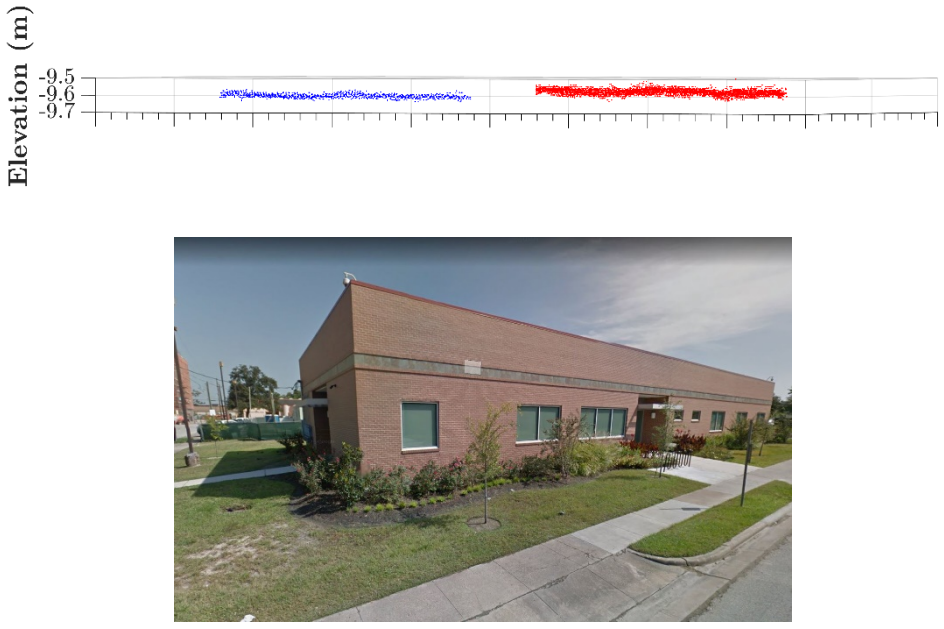

Figure 20: Profile of a sampled roof (~20 m wide, σ ~ 1 cm for LML, σ ~ 2.7 cm for SPL)

To better understand how other variables may be affecting these observed planar standard deviations, the mean intensity and angle of incidence were examined with respect to the planar fit standard deviations. The intensity values recorded by lidar systems are a measure of the strength of the returning laser pulse, and typically the peak amplitude is used. However, among lidar manufacturers, there is no standardized method of deriving this from the return signal. Furthermore, although intensity values are related to surface reflectivity, they are a relative measure affected by other variables such as acquisition geometry and the laser scanners themselves [62], [63]. Despite this, intensity values are useful for classification, object detection, and many other applications. Among many other possible sources of error, lidar range finder accuracy has been shown to decrease with low reflectivity, and thus low intensity, because the accuracy and precision of range estimation are proportional to the signal-to-noise ratio (SNR) [12], [48], [57]. With all other factors held equal (e.g., distance, atmosphere, and incidence angle), the strength of the returning signal depends on the surface reflectivity. Studies have found the range error associated with varying intensity values to be in the range of mm for LML [64], [65]. A recent study by Wujanz et al. (2017) found that in laboratory-controlled conditions, with calibration targets, the range error in a terrestrial lidar system decreased non-linearly as the recorded intensity increased [66].

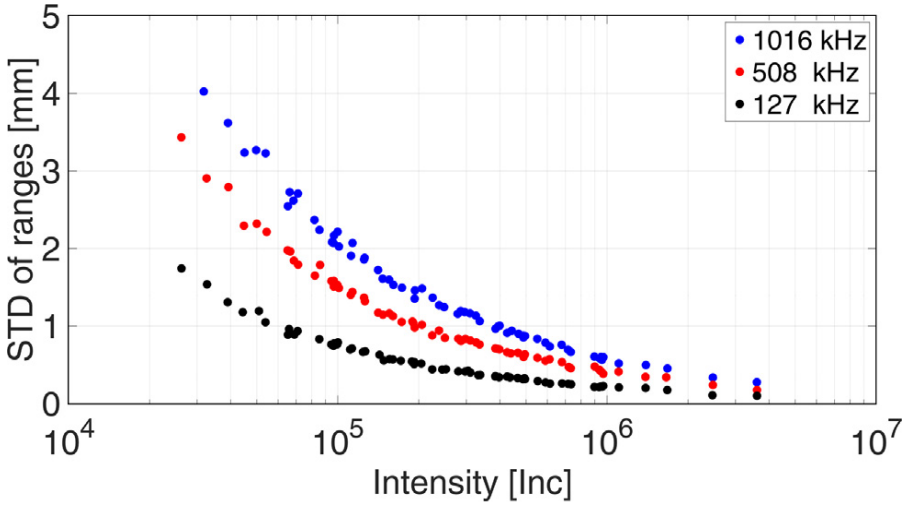

Figure 21: Intensity versus standard deviation of ranges (taken from Wujanz et al. 2017)

In their examination of recorded intensity versus ranging precision (standard deviation of recorded ranges), Wujanz et al. (2017) found the data fit a power function (Figure 21). Assuming that the behavior of real-world targets will bear some resemblance to those under laboratory-controlled conditions, the following equation was used to fit the planar standard deviations (σ) versus intensity (I), where a and b are unknown constant parameters:

$$\sigma = a \cdot I^b. \tag{5-1}$$

Although the data for the SPL100 had a high fit to the power function (R^2=0.658), the data from the Optech Titan were a poor fit ($R^2 < 0.3$) (Figure 22-24). The LML plots do show a non-linear relationship, and it is possible that under controlled conditions the data would exhibit a power function type relationship. There are several possible reasons for the poor fit in the LML data. Although the planar samples were chosen to be as homogeneous as possible, these regions may well have been a composite of several materials with different reflectivity properties. It is also possible that the targets chosen

did not represent the full dynamic range of the detectors. The 1550 nm channel, which had the poorest fit to the predicted behavior (R^2=0.136), also had the smallest range of intensity values (~150 – 4,200) as compared to the 532 nm channel, which had a slightly better fit (R^2=0.300) and the broadest range of intensity values (~350 – 10,000).

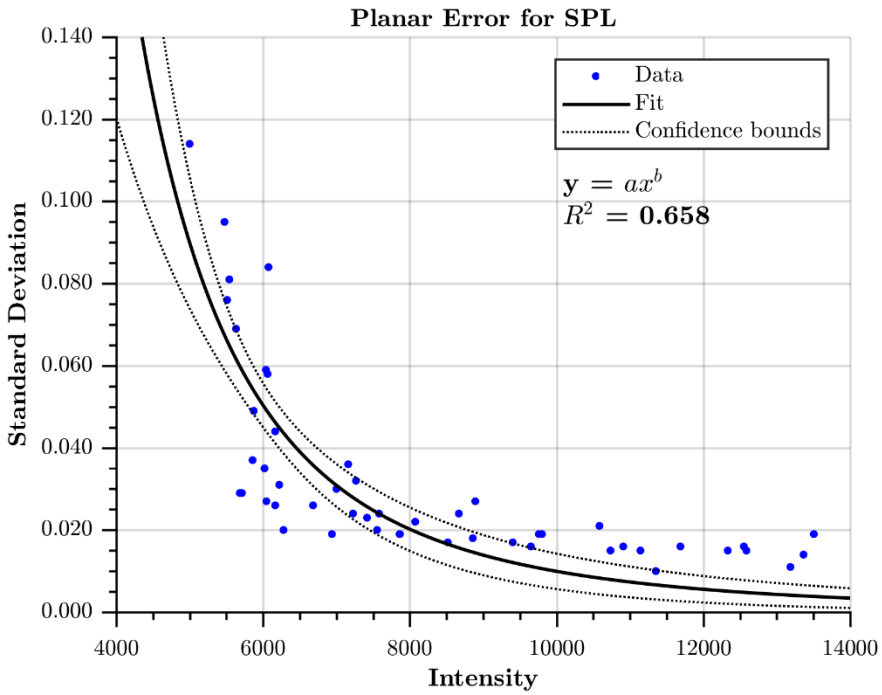

Figure 22: SPL100 intensity versus standard deviation

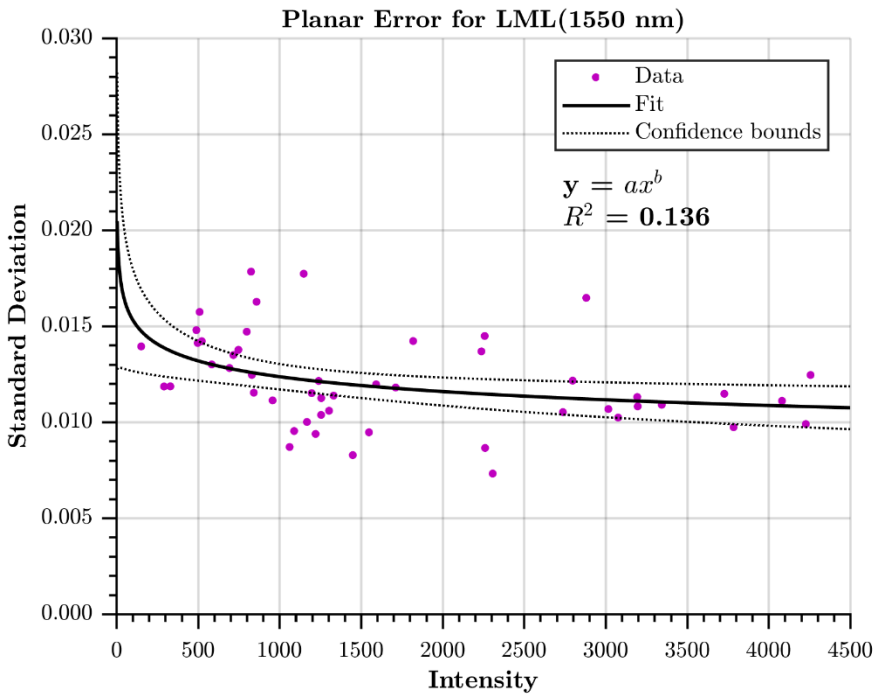

Figure 23: Optech Titan intensity (1550 nm) versus standard deviation

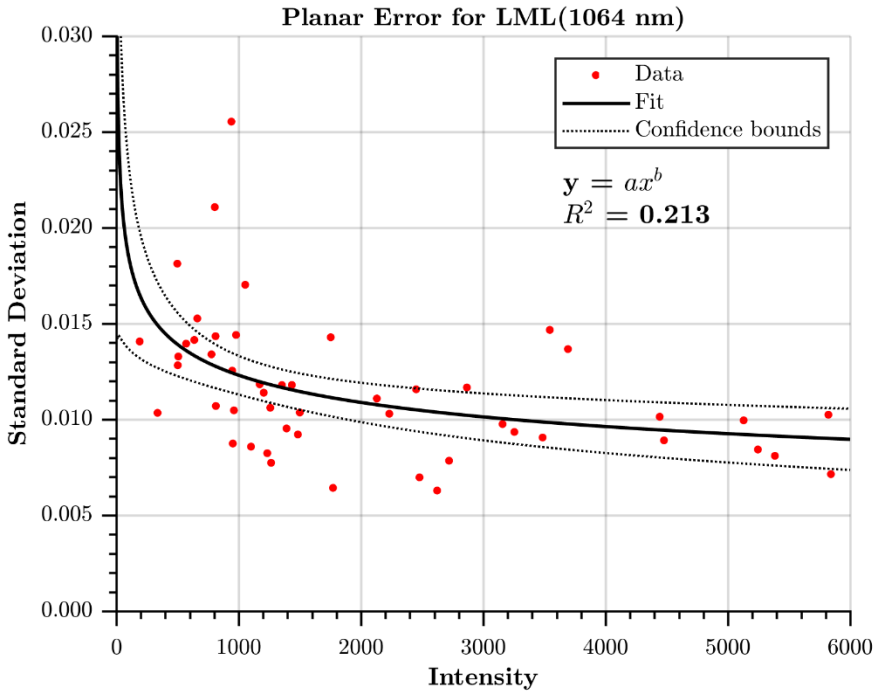

Figure 24: Optech Titan intensity (1064 nm) versus standard deviation

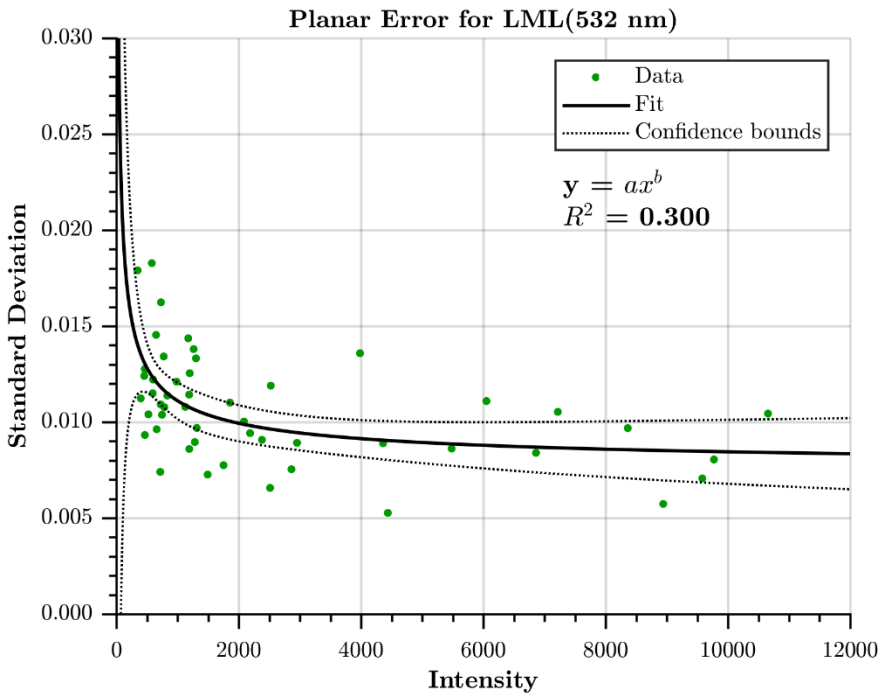

Figure 25: Optech Titan intensity (532 nm) versus standard deviation

Finally, the effects of the angle of incidence on the observed planar standard deviations were also considered. A ranging error can occur when a laser beam illuminates a surface at a non-normal angle. Baltsavias (1999) characterized the maximum range error, ΔR_{max} , that would occur at an angle of incidence θ for a given flying height (h) and beam divergence (γ) with the following equation [67]:

$$\Delta R_{max} = h\gamma \frac{|\tan\theta|}{2}. \qquad (5\text{-}2)$$

Using the above equation with a flying height of 3700 m and a beam diverge of 0.08 mrad/beamlet, the SPL100 would have a maximum expected range error of 26 cm for a 60° angle of incidence (Figure 26). For the infrared Optech Titan channels ($h = 500$, $\gamma = 0.35$ mrad), the error would be 15 cm. At 30°, this drops to 8.5 and 5 cm, respectively. These values are far in excess of what was observed in this study. At 60°, the SPL100

had planar standard deviations of about 8-10 cm, while in the Optech Titan it was about 1.5-2 cm. The Baltsavias equation appears to be a poor predictor for ranging uncertainty due to incidence angle as the magnitude of the effect appears to be much smaller. There is, however, a linear trend between the angle of incidence and planar standard deviation for both systems at all wavelengths (Figure 27-Figure 30), which is not dissimilar to the trend predicted by Equation 5-2 between 0° and 60°, albeit with a lower slope.

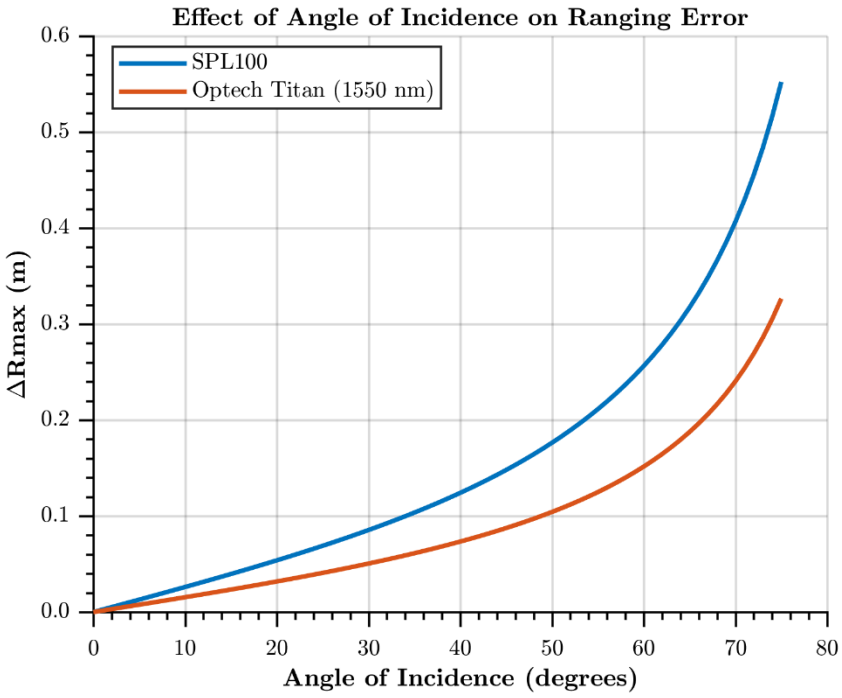

Figure 26: Theoretical Effect of Angle of Incidence on Ranging Error from Baltsavias (1999)

It is difficult to separate the effect of intensity and angle of incidence. For example, a high noise level could be explained by either a high reflectance surface recorded at a high incidence angle or a dark surface observed at a normal angle of incidence [66]. Furthermore, for a Lambertian surface, intensity decreases with the cosine of incidence

angle [68]. The resulting decrease in intensity, resulting in a lower SNR, will give rise a noisier measurement. When the angle of incidence and standard deviation are plotted together and colored by intensity values, it can be seen that the steeper angles were predominately darker targets (Figure 31, Figure 32). (Similar distributions were observed for all LML channels.)

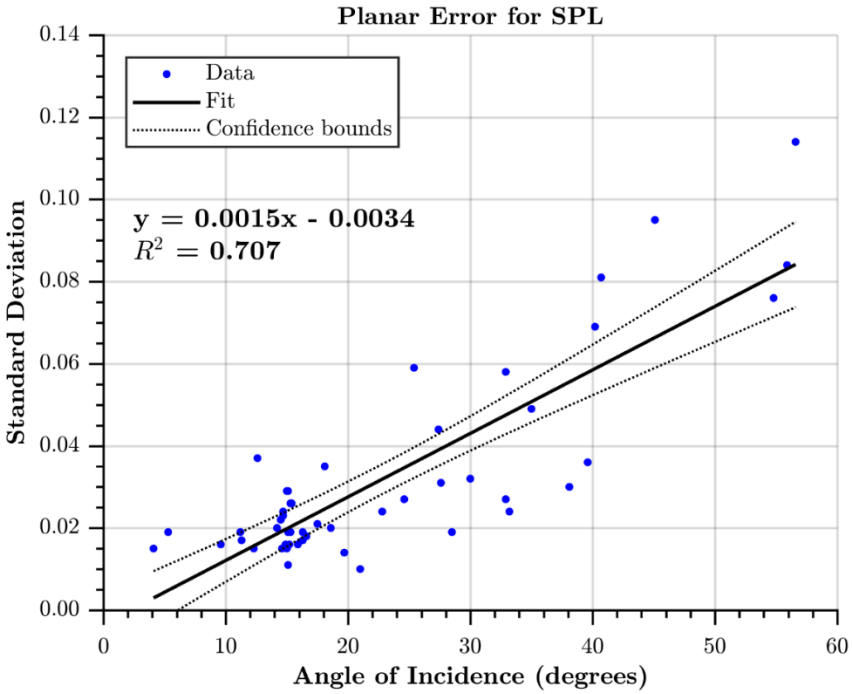

Figure 27: SPL100 Angle of Incidence versus Standard Deviation

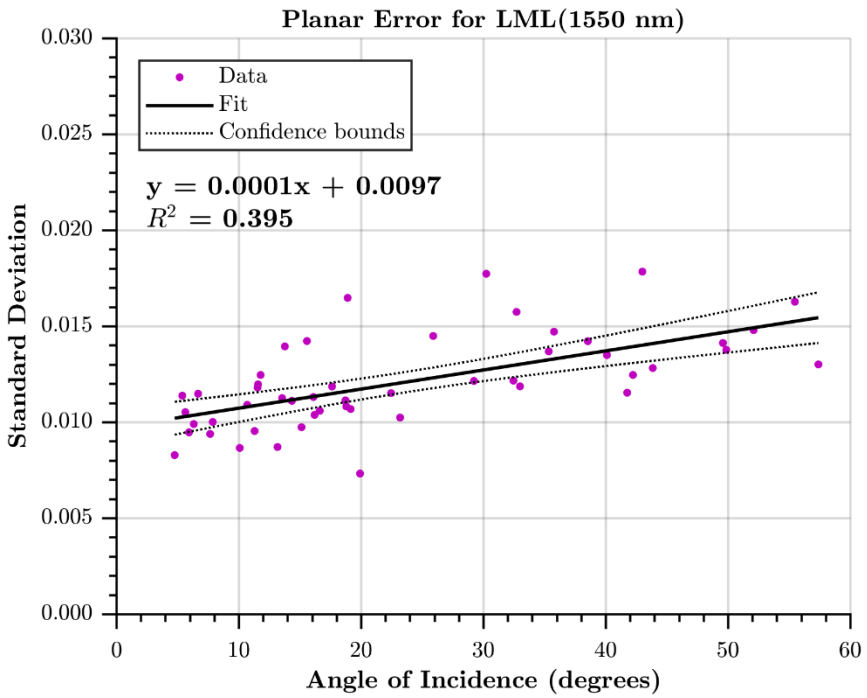

Figure 28: Optech Titan (1550 nm) Angle of Incidence versus Standard Deviation

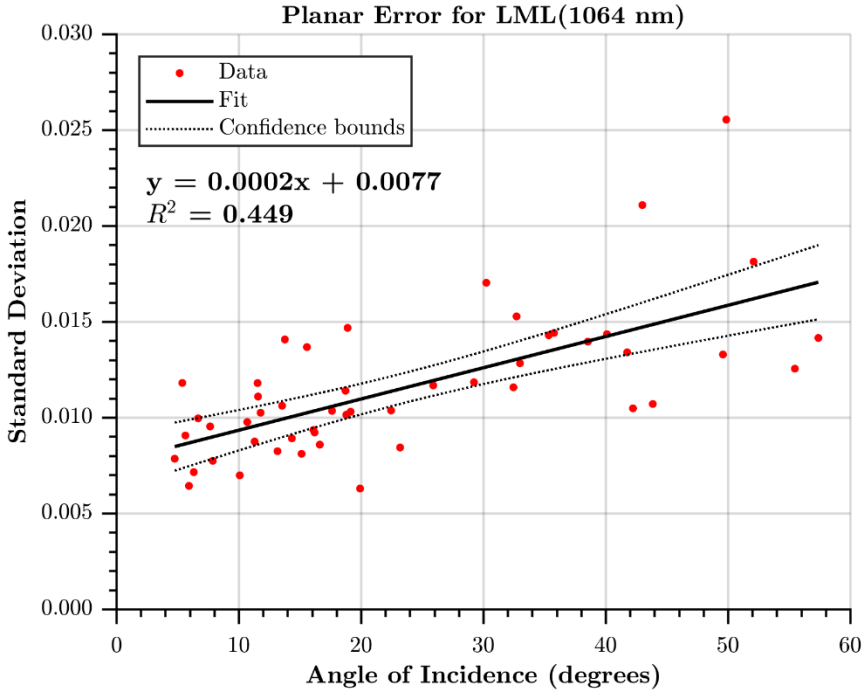

Figure 29: Optech Titan (1064 nm) Angle of Incidence versus Standard Deviation

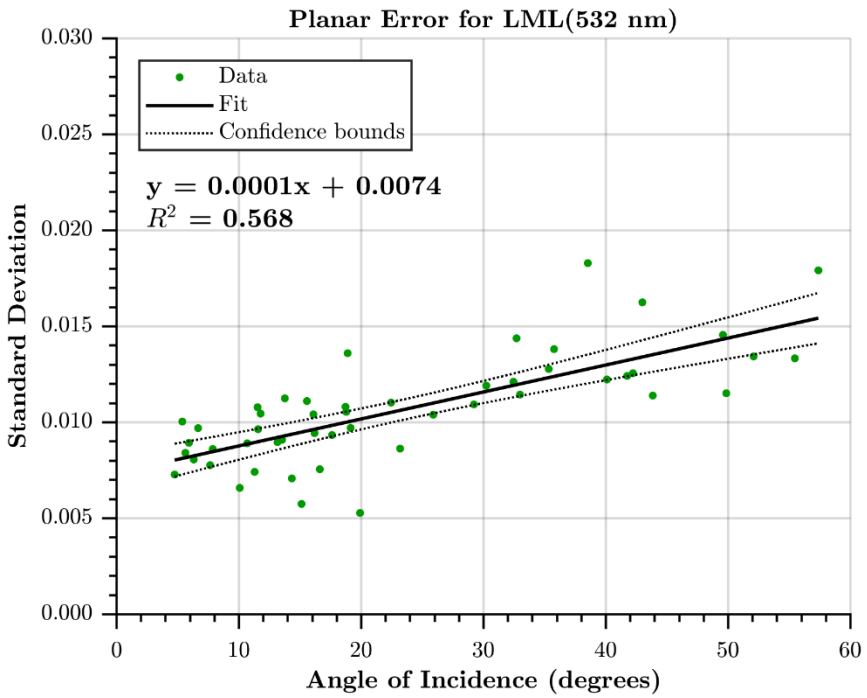

Figure 30: Optech Titan (532 nm) Angle of Incidence versus Standard Deviation

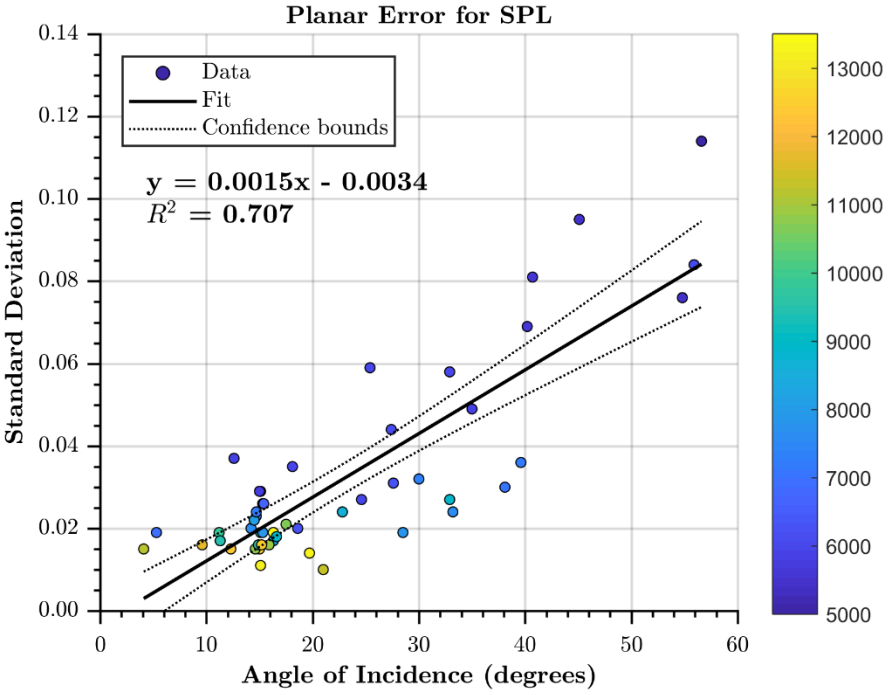

Figure 31: SPL100 plot of angle of incidence versus standard deviation, colored by intensity value

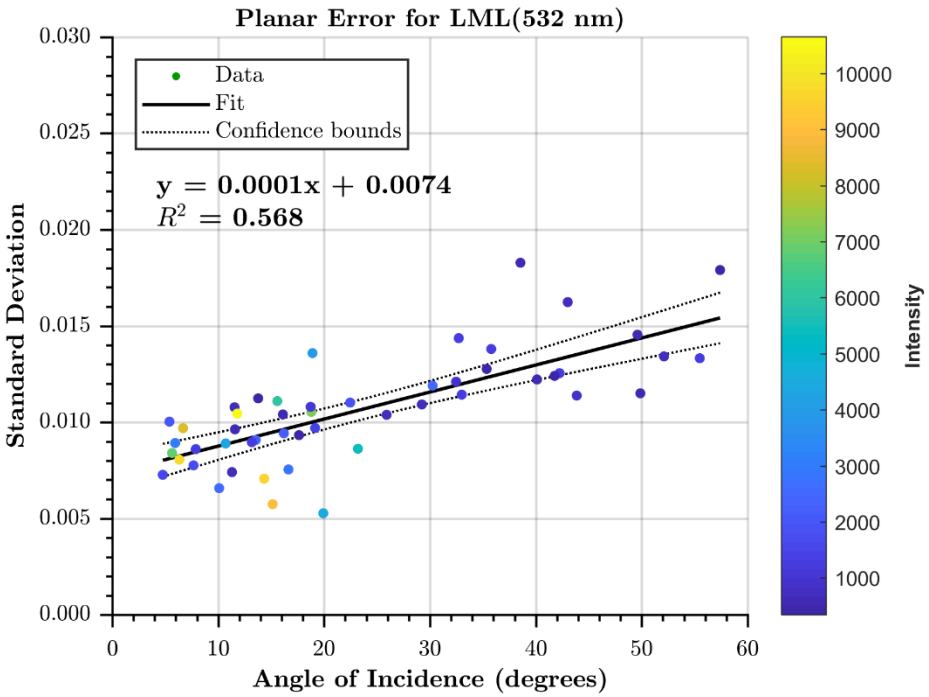

Figure 32: Optech Titan (532) plot of angle of incidence versus standard deviation, colored by intensity value

5.3 DEM Comparison

Thus far, the accuracy and precision analysis have been limited to GNSS spot checks and small planar patches. A DEM comparison between the LML and SPL data, however, provides a spatially continuous macro view of relative system performance that will reveal systematic differences. In Figure 33, two one-meter resolution maps show the difference between the DEMs derived from the Optech Titan and two SPL100 DEMs generated from data processed with two different versions of HxMap. There are artifacts visible in both images in areas with buildings due to slight differences and misclassifications from the ground classification routine. Furthermore, water bodies such as the bayou and man-made ponds differ in elevation between the SPL100 and Optech

Titan data because the ground classification routine did not identify the Optech Titan 532 nm bathymetry as ground returns, while the SPL bathymetry was identified as ground.

More significantly, the SPL100 point cloud derived from the HxMap software in 2017, when the lidar data was collected, contains noticeable artifacts at the edges of the SPL100 flight lines. At these edges, the SPL100 differs from the Optech Titan DEM by about 4 cm. Reprocessing the raw data in 2019 revealed that recent updates to the HxMap software have improved post-processed data quality. In the right side of Figure 33, with a 2019 version of HxMap, the flight line artifacts have been minimized, and the DEM is in closer agreement to the Optech Titan derived DEM. These visual observations are confirmed with a histogram of the DEM differences (Figure 34), which shows a mean bias of -2.5 cm between the Optech Titan DEM and the 2017 HxMap post-processed SPL100 data, and 1.4 cm using the most recent version (2019) of HxMap software.

Given that the SPL100 is marketed for large area terrain mapping, it should be capable of producing DEMs that are of comparable quality and accuracy to those currently produced from traditional LML systems. The close agreement between the SPL100 DEM produced from the most recent version of HxMap and the Optech Titan DEM indicates that the SPL100 largely meets these requirements, but small systematic problems still exist at SPL flight line edges. There is an increased point density where flight lines overlap, and errors may occur when near-surface points from residual calibration errors or post-processing filtering bias the DEM. The updated HxMap workflow includes a decimation filter to produce a more homogeneous point density, which appears to reduce the artifacts at flight edges.

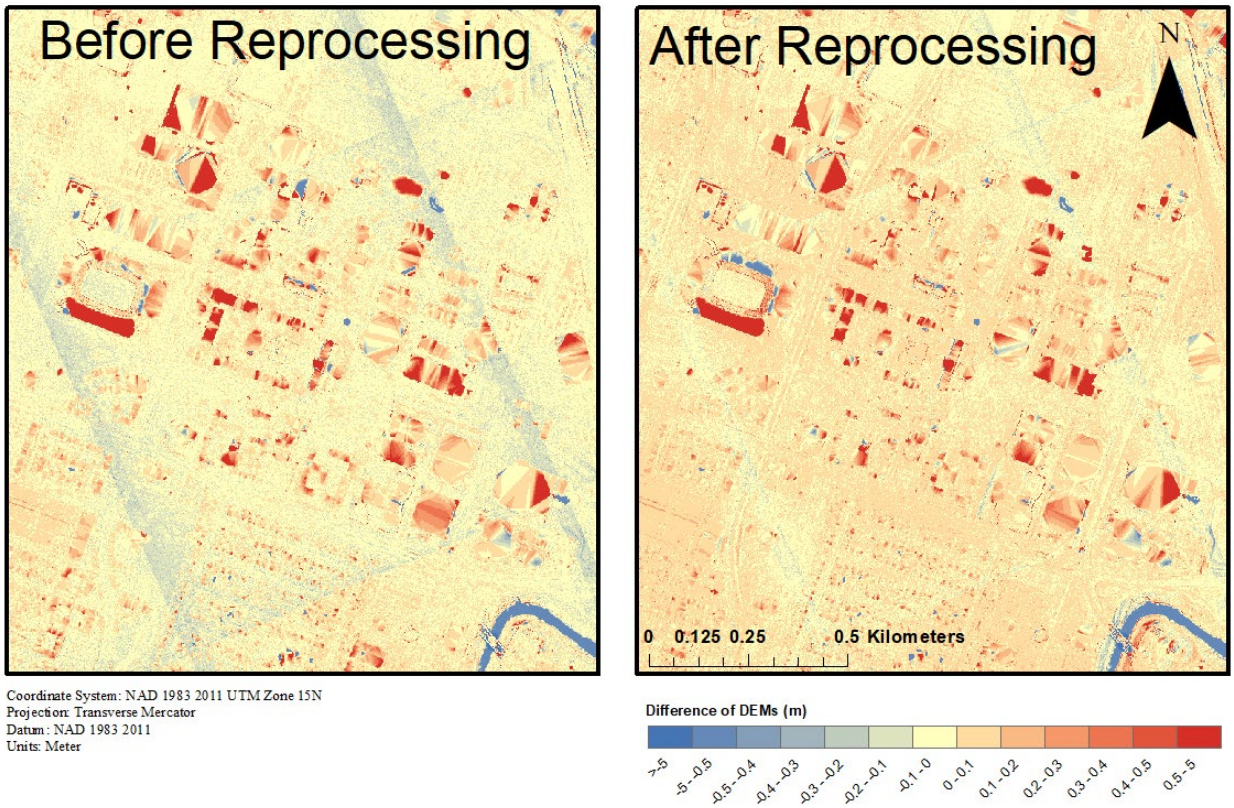

Figure 33: Difference of DEMs using 2017 HxMap software (left) and after using updated 2019 software (right)

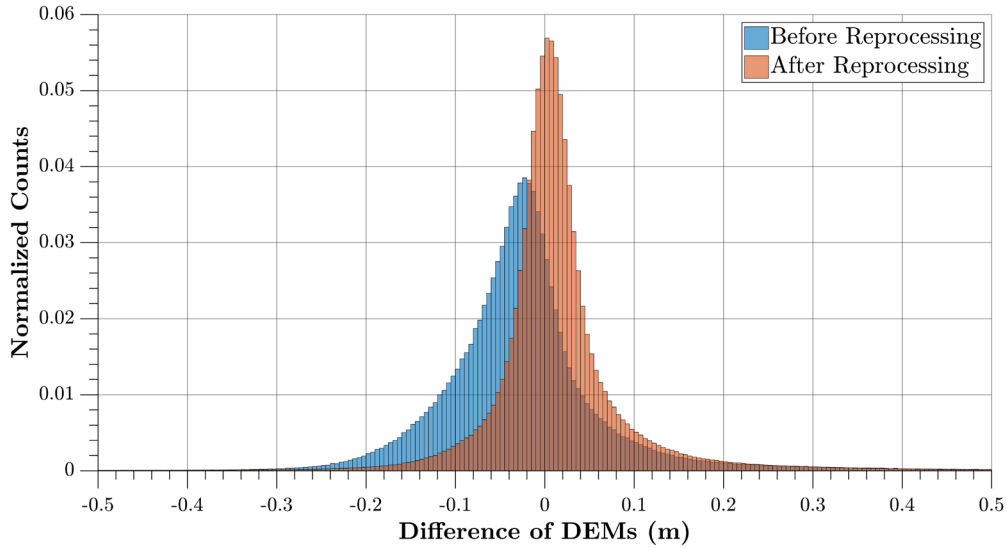

Figure 34: Histogram of the difference of DEMs between LML and SPL data

5.4 Canopy Performance

Both the Optech Titan and SPL100 are capable of capturing tree canopy structure and underlying ground surfaces (Figure 35, Figure 36), but their distinct detection methodologies result in considerably different underlying data characteristics. This study examined the ability of these systems to produce multiple returns and to penetrate through to the ground under tree canopies, as well as the minimum vertical separation possible with multiple returns, which is referred to as range resolution. Statistics describing these characteristics, generated from thirty sample canopy areas, are shown in Table 6. It can be readily observed that even though the SPL100 produces more detected laser pulses than the Optech Titan, the Titan generates more multiple and ground returns as a percentage of the total pulses.

Table 6: Canopy Performance Statistics

	Avg. Number of Pulses	% Multiple Returns	% Ground Returns	Avg. Vertical Separation from Return 1 to 2
Optech Titan	~ 17,000	87%	71%	4.3 m
SPL100	~ 36,000	22%	43%	9.9 m

Of the thirty sampled tree canopies, only 22% of SPL100 pulses had multiple returns, as compared to 87% for the Optech Titan. The Optech Titan, which is a discrete return lidar system, can record up to four returns per pulse. In this dataset, the SPL100, however, usually generates only one or two returns through the canopy. Although some pulses had three returns, this made up less than 1% of the total pulses analyzed. In contrast, pulses with three or four returns comprised 50% of the total pulses in the Optech Titan samples.

Figure 35: Trees representing samples (A) and (C), on left, and trees representing samples (B) and (D), on the right, that are depicted in Figure 36 and Figure 37

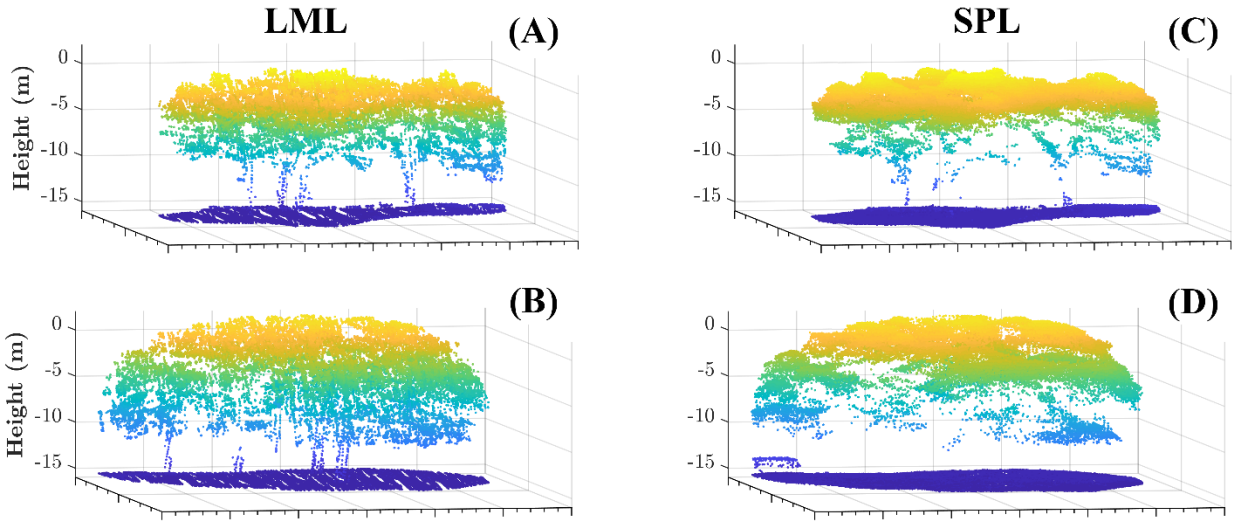

Figure 36: Canopy structure in Optech Titan point cloud (left) and SPL100 (right)

It is apparent that in terms of range resolution, the SPL100 is considerably more limited than an LML system. On average, the first and second returns had about 10 m of vertical separation, and only a small fraction of the second returns came from lower in the canopy. Visual inspection of the point cloud, colored by return number, and the

histogram of range separations shows that the second returns in the SPL100 are overwhelmingly from the ground (Figure 37, Figure 38). The first and second returns in the Optech Titan are separated, on average, by 4.3 m. This average, however, comes from a bimodal distribution made of up second returns from the canopy and on the ground. These observations are in agreement with the study from Mandlburger et al. (2019), which found that the SPL100 had on average 1.06 returns through thick vegetation, as compared to 1.84 mean returns using a full-waveform lidar system [15].

Previous studies on the SPL100's predecessor, HRQLS, specify that the system has a 1.6 ns pixel recovery time, and is thus capable of recording returns separated by 24 cm [3], [4]. The SPL100 range resolution is not held back by inherent detector limitations, but rather due to noise filtering. During post-processing, a dead distance filter is applied to the SPL100 data to eliminate after-pulsing noise [69]. However, this filter also removes a significant amount of multiple returns, which are necessary for adequate canopy penetration. Mandlburger et al. (2019) also postulated that noise filtering during post-processing removed valid multi-returns in the canopy [15]. The range resolution of unfiltered SPL100 data was analyzed to validate this assumption. Unfiltered SPL data, however, has a large column of noise extending above and below the surface returns. To get around this limitation, any noise points above the canopy or below the ground level were removed. The return numbers of the remaining points were then adjusted so that first returns could only occur within the bounding box.

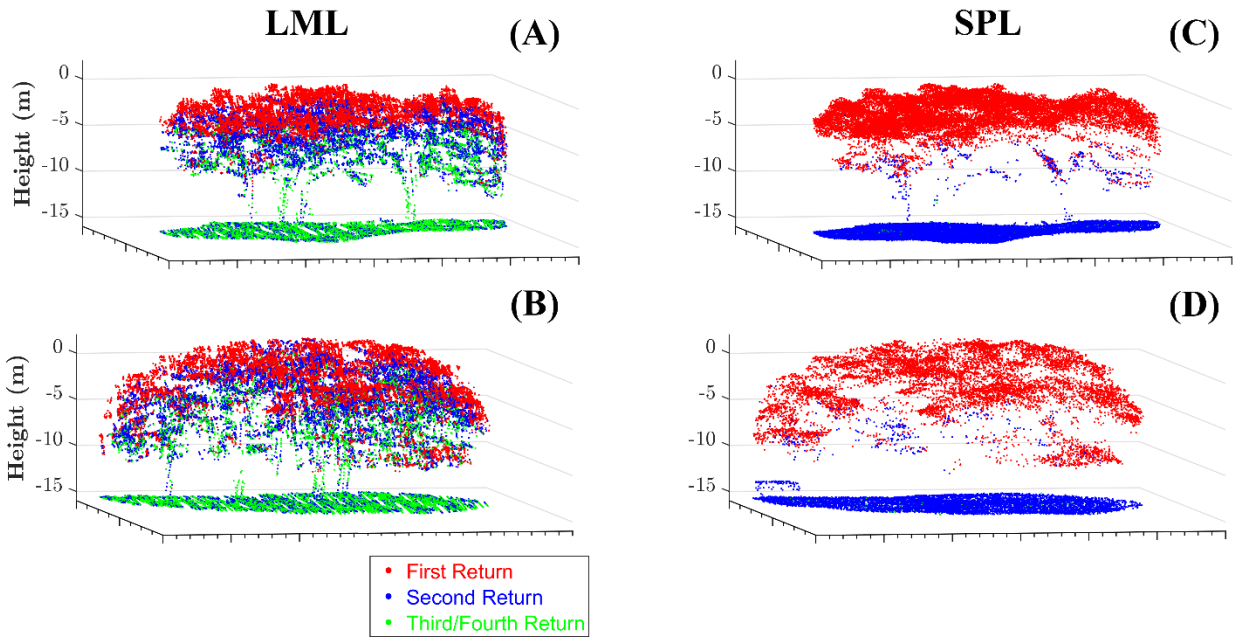

Figure 37: Multiple returns in tree canopy for Optech Titan (left) and SPL100 (right)

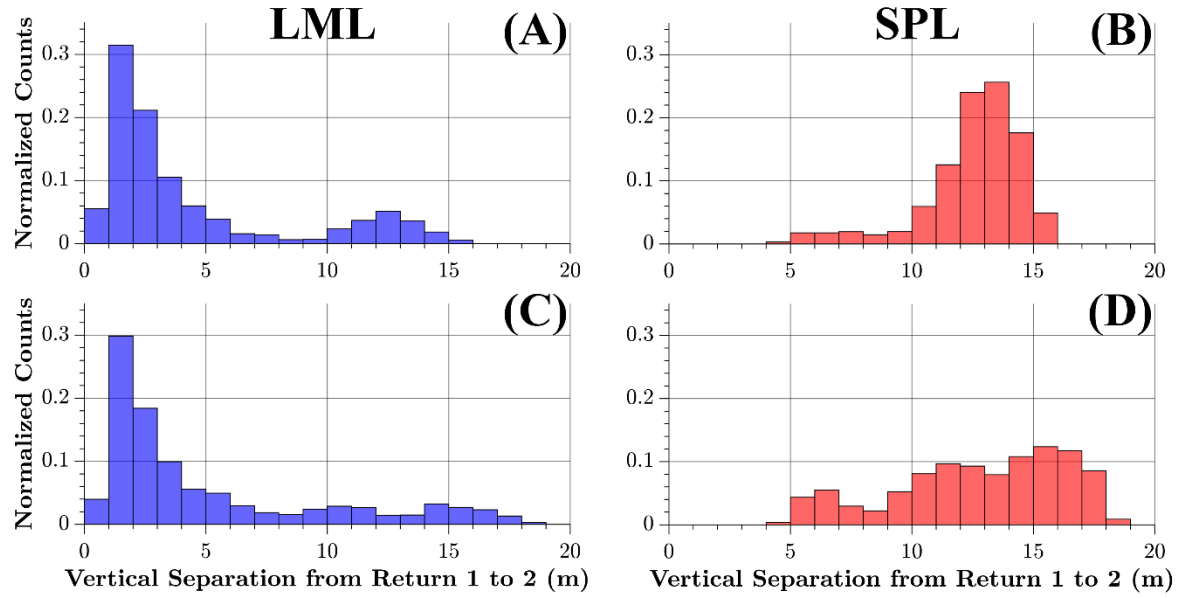

Figure 38: Histograms of range distance between first and second returns for Optech Titan (left) and SPL100 (right)

As depicted in Figure 39, the unfiltered SPL100 has multiple returns distributed throughout the canopy. On average, the first and second returns in an unfiltered SPL100 point cloud are separated by 4.0 m, which is slightly better than what was observed with LML data. This average, of course, does include the separation between multiple returns in the canopy and between valid returns and noise points. These results confirm that SPL100 range resolution is presently limited by noise filtering. In the future, Leica could possibly address this with more sophisticated filtering algorithms that would reduce noise while better preserving multiple returns through vegetation.

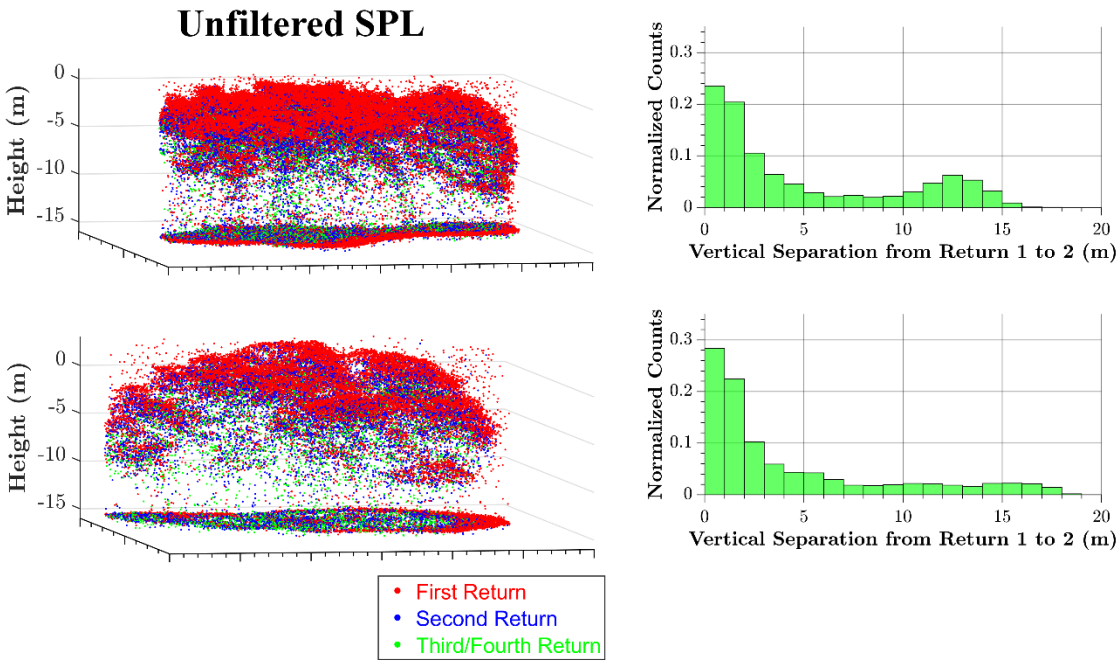

Figure 39: Multiple returns in tree canopy for unfiltered SPL100 point clouds

In addition to producing more pulses with multiple returns, more of the pulses reached the ground with the Optech Titan (71%) than in the post-processed SPL100 (44%). However, the reason the SPL100 is capable of generating higher ground densities under tree canopies, as compared to the Optech Titan, is due to the higher number of lidar measurements rather than superior penetration performance. For the samples tested here, the LML data had a point density of about 10 pts/m^2 under the treetops while the SPL data had about 28 pt/m^2, but at the flight edges, this can increase to over 100 pt/m^2. In the Mandlburger et al. study, which planned their data acquisitions to achieve similar overall point density (20 points/m^2), the full-waveform lidar point density under vegetation surpassed that of the SPL100 [15]. In general, an LML sensor with a higher ground sampling rate will surpass the SPL for ground density under the canopy.

Lastly, this analysis of canopy performance considered the ranging precision of flat terrain under the treetops as compared to adjacent areas of open terrain with roughly the same land cover. Surprisingly, the SPL100 did not exhibit a large decrease in precision under treetops, as Stoker et al. (2016) had noted a drop in vertical accuracy under canopy [4]. Under canopy cover, flat terrain had an overall standard deviation of 3.6 cm (computed from all residuals for 25 samples) and 3.0 cm in open terrain (Table 7). In contrast, the Optech Titan fell from 2.7 cm under the canopy to nearly half that, 1.7 cm, in open terrain. A two-sample F-test determined that for both systems, differences in planar variances were statistically significant at 95% when comparing the residuals of samples under the canopy and those in open terrain.

These results are roughly in line with the Mandlburger et al. (2019), although they did not look into standard deviation statistics under the canopy. They found that the

SPL100 had a dispersion of about 3.9 cm in open meadows while in a full-waveform LML system, it was 1.0 cm [15]. In their examination of the HRQLS's ability to meet the needs of the USGS, Stoker, et al. (2016) raised concerns that the vertical accuracy in vegetated areas for the bare-earth DEMs was unacceptable during leaf-on conditions [4]. The reduced accuracy was attributed to noisier points and larger voids under the canopy as compared to LML. The results presented here, however, are not directly comparable due to differences in study sites. The study from Stoker et al. considered both a forested region in addition to an urban area, while this analysis looked mainly at small groves of trees in urban areas, typically with manicured lawns underneath. Only a few areas of denser tree cover, such as parks and empty lots, were included. Further research is needed to test whether the SPL100 is capable of acceptable accuracy under dense canopy for non-urban areas.

Table 7: Standard Deviation of Terrain under Canopy

	Std Dev Under Canopy (cm)	Std Dev Open Terrain (cm)
Optech Titan	2.7	1.5
SPL100	3.6	3.0

6. Conclusion

The Leica SPL100, which utilizes a detector array of many single photon sensitive elements, is capable of large data acquisition rates while maintaining superior point density as compared to the traditional linear mode lidar (LML) systems on the market. The results shown in this thesis validate theoretical expectations of lower ranging precision in the SPL100 than in LML, and also demonstrate how the precision is more negatively affected by surface properties such as low intensity, roughness, and slope [11], [12], [15], [43]. For the fifty planar surfaces tested, the SPL100 shows a much larger range of standard deviations, from 1 cm up to 11 cm. The LML data, collected with an Optech Titan, had planar standard deviations that only ranged from 0.5 to 3 cm. Taking the residuals of all the samples together, the SPL100 had an overall standard deviation of 3.2 cm, while in the Optech Titan it was only 1.2 cm. Even though the SPL100 was flown from a significantly higher flying height, and has worse ranging precision, GNSS survey data found that the post-processed SPL100 point cloud has similar positional accuracy to that of the LML data, at least for the smooth, flat surfaces tested. Furthermore, the DEM derived from the SPL100 closely agrees with the DEM produced from the Optech Titan; the mean difference between the two DEMS was 1.4 cm. Although recent updates to Leica's HxMap have improved post-processed data quality, biases at the SPL100 flight line edges remain visible in the difference of DEM image.

System performance under tree canopy was also considered. In vegetation, only one or two returns are to be expected from the post-processed SPL100 data. In the samples tested, the first and second returns had, on average, a vertical separation of about 10 m. Most of the second returns came from the ground, rather than lower in the canopy. In

contrast, the Optech Titan, a discrete return LML system, can record up to four returns per outgoing pulse. Multiple returns are well distributed throughout the canopy. The first and second returns in the Optech Titan are separated, on average, by 4.3 m. Analysis of unfiltered SPL100 data confirmed that noise filtering during post-processing was the primary reason for the poor range resolution in the SPL100 as the algorithm removes a portion of the multiple returns. The unfiltered data set had a similar ability to resolve multiple returns as the LML, with an average of 4.0 m between the first and second returns within the canopy. In the future, more sophisticated noise-filtering algorithms may be able to preserve valid returns better while removing spurious noise points. Despite its limited range resolution, the high point densities of the post-processed SPL100 data do, however, permit tree canopies to be reconstructed with enough accuracy to allow for variables such as tree heights and biomass to be measured [5], [19]. Under the canopy, the SPL100 had a planar standard deviation of 3.6 cm while in the Optech Titan it was 2.7 cm. Although Stoker et al. raised concerns about vertical accuracy under vegetation with the HRQLS, differences in study sites did not allow for a direct comparison of results.

In its current state, the SPL100 is likely best suited for applications in which the need for data collection efficiency outweighs the need for the best possible accuracy and precision. Despite its lower ranging precision and higher rates of false returns, the SPL100 is nonetheless capable of accuracy similar to LML[4], [15]. Additionally, for some users, the SPL100's lack of full-waveform information and being restricted to using a laser wavelength in the visible light may also present a significant disadvantage as compared to the wide variety of LML systems available.

Going forward, single photon lidar and Geiger-mode lidar systems will benefit from additional research so that users of these new technologies will have a thorough understanding of best practices for data collection and processing. In particular, future studies should focus on the SPL100's positional accuracy on sloped and textured surfaces, including terrain under vegetation cover. It has been demonstrated here in this thesis and elsewhere that such conditions significantly worsen ranging position, but more information is needed to quantify its effect on accuracy. The SPL100's suitability for forestry applications should also be examined in light of the knowledge that noise filtering removes returns in the canopy. The SPL100 is a promising new sensor for efficient large-area mapping, but given that its detection capabilities are very different from traditional LML systems, it is crucial to understand its performance limitations and in what conditions they occur.

The use of SPL and GML for commercial surveying and mapping is not yet a mature technology. It is expected that the SPL100 capabilities will continue to improve from what is reported here. In 2016, for example, the study by Stoker et al. critiqued the HRQLS for not providing point clouds with time stamp, multiple returns, or intensity information [4]. The SPL100 that is now available for commercial use has addressed all these deficiencies, however. The DEM comparison presented in this thesis, likewise, indicates that the Leica software for post-processing the SPL100 data is also being refined. It is thus possible, likely even, that future hardware or software changes will bring the SPL100 closer into line with the precision and accuracy that is now available from an LML system.

References

[1] J. Shan and C. K. Toth, Eds., *Topographic Laser Ranging and Scanning: Principles and Processing*. CRC Press, 2009.

[2] C. L. Glennie, W. E. Carter, R. L. Shrestha, and W. E. Dietrich, "Geodetic imaging with airborne LiDAR: the Earth's surface revealed," *Rep. Prog. Phys.*, vol. 76, no. 8, p. 086801, Jul. 2013.

[3] J. Degnan, "Scanning, Multibeam, Single Photon Lidars for Rapid, Large Scale, High Resolution, Topographic and Bathymetric Mapping," *Remote Sensing*, vol. 8, no. 11, p. 958, Nov. 2016.

[4] J. M. Stoker, Q. A. Abdullah, A. Nayegandhi, and J. Winehouse, "Evaluation of Single Photon and Geiger Mode Lidar for the 3D Elevation Program," *Remote Sensing*, vol. 8, no. 9, p. 767, Sep. 2016.

[5] A. Swatantran, H. Tang, T. Barrett, P. DeCola, and R. Dubayah, "Rapid, High-Resolution Forest Structure and Terrain Mapping over Large Areas using Single Photon Lidar," *Scientific Reports*, vol. 6, p. 28277, Jun. 2016.

[6] Leica Geosystems, "Leica SPL100 Single Photon LiDAR Sensor." [Online]. Available: https://leica-geosystems.com/en/products/airborne-systems/lidar-sensors/leica-spl100. [Accessed: 07-Jun-2018].

[7] J. Degnan and C. T. Field, "Moderate to high altitude, single photon sensitive, 3D imaging lidars," in *Advanced Photon Counting Techniques VIII*, 2014, vol. 9114, p. 91140H.

[8] J. Degnan, R. Machan, E. Leventhal, D. Lawrence, G. Jodor, and C. Field, “Inflight performance of a second-generation photon-counting 3D imaging lidar,” in *Laser Radar Technology and Applications XIII*, 2008, vol. 6950, p. 695007.

[9] Hexagon, “Hexagon acquires SigmaSpace Corporation, a leading 3D mapping company [Press Release],” 18-Feb-2016. [Online]. Available: https://hexagon.com/news/press-releases/press-release-detail-page?alertID=1392370. [Accessed: 07-Jun-2018].

[10] Leica Geosystems, “New Leica SPL100 brings up to 10x more efficiency to airborne LiDAR mapping,” 13-Feb-2017. [Online]. Available: https://leica-geosystems.com/en/about-us/news-room/news-overview/2017/02/2017-02-13-new-leica-spl100-brings-up-to-10x-more-efficiency-to-airborne-lidar-mapping. [Accessed: 07-Jun-2018].

[11] A. Ullrich and M. Pfennigbauer, “Linear LIDAR versus Geiger-mode LIDAR: impact on data properties and data quality,” in *Laser Radar Technology and Applications XXI*, 2016, vol. 9832, p. 983204.

[12] A. Ullrich and M. Pfennigbauer, “Noisy lidar point clouds: impact on information extraction in high-precision lidar surveying,” in *Laser Radar Technology and Applications XXIII*, 2018, vol. 10636, p. 106360M.

[13] W. E. Clifton, B. Steele, G. Nelson, A. Truscott, M. Itzler, and M. Entwistle, “Medium altitude airborne Geiger-mode mapping LIDAR system,” in *Laser Radar Technology and Applications XX; and Atmospheric Propagation XII*, 2015, vol. 9465, p. 946506.

[14] B. Jutzi, “Less Photons for More LiDAR? A Review from Multi-Photon Detection to Single Photon Detection,” in *56th Photogrammetric Week 2017*, Stuttgart, Germany, 2017.

[15] G. Mandlburger, H. Lehner, and N. Pfeifer, “A Comparison of Single Photon and Full Waveform LiDAR,” *ISPRS Annals of the Photogrammetry, Remote Sensing and Spatial Information Sciences*, vol. IV-2/W5, 2019.

[16] A. M. Kim, S. C. Runyon, and R. C. Olsen, “Comparison of full-waveform, single-photon sensitive, and discrete analog LIDAR data,” in *Laser Radar Technology and Applications XX; and Atmospheric Propagation XII*, 2015, vol. 9465, p. 94650L.

[17] H. K. Heidemann, “Lidar base specification,” U.S. Geological Survey, Reston, VA, USGS Numbered Series 11-B4, 2012.

[18] G. Mandlburger and B. Jutzi, “On the Feasibility of Water Surface Mapping with Single Photon LiDAR,” *ISPRS International Journal of Geo-Information*, vol. 8, no. 4, p. 188, Apr. 2019.

[19] A. Wästlund, J. Holmgren, E. Lindberg, and H. Olsson, “Forest Variable Estimation Using a High Altitude Single Photon Lidar System,” *Remote Sensing*, vol. 10, no. 9, p. 1422, Sep. 2018.

[20] S. Higgins, “Dr. Andreas Ullrich on Waveform Lidar vs Single-Photon and Geiger-Mode,” *SPAR 3D*, 18-Jan-2017. [Online]. Available: https://www.spar3d.com/blogs/the-other-dimension/riegls-dr-andreas-ullrich-waveform-lidar-vs-single-photon-geiger-mode/. [Accessed: 03-Jun-2019].

[21] E. P. Baltsavias, E. Favey, A. Bauder, H. Bosch, and M. Pateraki, “Digital Surface Modelling by Airborne Laser Scanning and Digital Photogrammetry for Glacier Monitoring,” *The Photogrammetric Record*, vol. 17, no. 98, pp. 243–273, 2001.

[22] K.-H. Thiel and A. Wehr, “Advanced processing capabilities with imaging laser altimeter ScaLARS,” in *Laser Radar Technology and Applications IV*, 1999, vol. 3707, pp. 46–57.

[23] A. Wehr and U. Lohr, “Airborne laser scanning—an introduction and overview,” *ISPRS Journal of Photogrammetry and Remote Sensing*, vol. 54, no. 2, pp. 68–82, Jul. 1999.

[24] D. Harding, “Pulsed Laser Altimeter Ranging Techniques and Implications for Terrain Mapping,” in *Topographic Laser Ranging and Scanning: Principles and Processing*, J. Shan and C. K. Toth, Eds. CRC Press, 2009, pp. 173–194.

[25] C. Mallet and F. Bretar, “Full-waveform topographic lidar: State-of-the-art,” *ISPRS Journal of Photogrammetry and Remote Sensing*, vol. 64, no. 1, pp. 1–16, Jan. 2009.

[26] W. Wagner, A. Ullrich, V. Ducic, T. Melzer, and N. Studnicka, “Gaussian decomposition and calibration of a novel small-footprint full-waveform digitising airborne laser scanner,” *ISPRS Journal of Photogrammetry and Remote Sensing*, vol. 60, no. 2, pp. 100–112, Apr. 2006.

[27] Z. Pan, J. C. Fernandez-Diaz, C. L. Glennie, and M. Starek, “Shallow water seagrass observed by high resolution full waveform bathymetric LiDAR,” in *2014 IEEE Geoscience and Remote Sensing Symposium*, 2014, pp. 1341–1344.

[28] J. Riu, M. Sicard, S. Royo, and A. Comerón, “Silicon photomultiplier detector for atmospheric lidar applications,” *Opt. Lett., OL*, vol. 37, no. 7, pp. 1229–1231, Apr. 2012.

[29] R. Heinrichs, B. Aull, R. Marino, D. Fouche, A. McIntosh, J. Zayhowski, T. Stephens, M. O'Brien, M. Albota, “Three-dimensional laser radar with APD arrays,” in *Laser Radar Technology and Applications VI*, 2001, vol. 4377, pp. 106–118.

[30] Hamamatsu Photonics K.K, “Avalanche photodiodes (APD) and silicon photomultipliers (SiPM),” in *Opto-semiconductor Handbook*, Hamamatsu Photonics K.K, 2014.

[31] G. Barbarino, R. De Asmundis, G. De Rosa, C. M. Mollo, S. Russo, and D. Vivolo, “Silicon Photo Multipliers Detectors Operating in Geiger Regime: an Unlimited Device for Future Applications, Photodiodes,” in *Photodiodes- World Activities in 2011*, J. W. Park, Ed. InTech, 2011.

[32] P. Hartzell, Z. Dang, Z. Pan, and C. Glennie, “Radiometric Evaluation of an Airborne Single Photon Lidar Sensor,” *IEEE Geoscience and Remote Sensing Letters*, pp. 1–5, 2018.

[33] Hamamatsu Photonics K. K., *Photomultiplier Tube Handbook*, 3a ed. Hamamatsu Photonics K. K., 2007.

[34] T. Gys, “Micro-channel plates and vacuum detectors,” *Nuclear Instruments and Methods in Physics Research Section A: Accelerators, Spectrometers, Detectors and Associated Equipment*, vol. 787, pp. 254–260, Jul. 2015.

[35] J. L. Wiza, “Microchannel plate detectors,” *Nuclear Instruments and Methods*, vol. 162, no. 1, pp. 587–601, Jun. 1979.

[36] A. Ghassemi, K. Sato, and K. Kobayashi, “Multi-Pixel Photon Counter,” Hamamatsu Photonics K.K., Technical Note, Mar. 2017.

[37] SensL, “An Introduction to the Silicon Photomultiplier,” Technical Note, 2011.

[38] R. Agishev, A. Comerón, J. Bach, A. Rodriguez, M. Sicard, J. Riu, S. Roy, “Lidar with SiPM: Some capabilities and limitations in real environment,” *Optics & Laser Technology*, vol. 49, pp. 86–90, Jul. 2013.

[39] D. Renker, “Geiger-mode avalanche photodiodes, history, properties and problems,” *Nuclear Instruments and Methods in Physics Research Section A: Accelerators, Spectrometers, Detectors and Associated Equipment*, vol. 567, no. 1, pp. 48–56, Nov. 2006.

[40] N. Otte, “The silicon photomultiplier-a new device for high energy physics, astroparticle physics, industrial and medical applications.,” in *Proceedings to SNIC symposium*, Stanford, California, 2006.

[41] Z. Pan, P. Hartzell, and C. Glennie, “Calibration of an Airborne Single-Photon Lidar System With a Wedge Scanner,” *IEEE Geoscience and Remote Sensing Letters*, vol. 14, no. 8, pp. 1418–1422, Aug. 2017.

[42] “The evolution of LiDAR.” [Online]. Available: https://leica-geosystems.com/about-us/news-room/customer-magazine/reporter-80/the-evolution-of-lidar. [Accessed: 10-Jun-2019].

[43] R. A. Barton-Grimley, J. P. Thayer, and M. Hayman, “Nonlinear target count rate estimation in single-photon lidar due to first photon bias,” *Opt. Lett., OL*, vol. 44, no. 5, pp. 1249–1252, Mar. 2019.

[44] Y. Yang, A. Marshak, S. P. Palm, T. Varnai, and W. J. Wiscombe, "Cloud Impact on Surface Altimetry From a Spaceborne 532-nm Micropulse Photon-Counting Lidar: System Modeling for Cloudy and Clear Atmospheres," *IEEE Transactions on Geoscience and Remote Sensing*, vol. 49, no. 12, pp. 4910–4919, Dec. 2011.

[45] C. Glennie, "Rigorous 3D error analysis of kinematic scanning LIDAR systems," *Journal of Applied Geodesy*, vol. 1, no. 3, pp. 147–157, 2008.

[46] T. Goulden and C. Hopkinson, "The Forward Propagation of Integrated System Component Errors within Airborne Lidar Data," *Photogrammetric Engineering & Remote Sensing*, vol. 76, no. 5, pp. 589–601, May 2010.

[47] K. W. Morin, "Calibration of airborne laser scanners," Masters thesis, University of Calgary, 2002.

[48] P. Schaer, J. Skaloud, S. Landtwing, and K. Legat, "Accuracy Estimation for Laser Point Cloud Including Scanning Geometry," *Mobile Mapping Symposium 2007, Padova*, 2007.

[49] J. J. Degnan, "A conceptual design for a spaceborne 3D imaging lidar," *Elektrotech. Inftech.*, vol. 119, no. 4, pp. 99–106, Apr. 2002.

[50] Z. Pan, "SPL100 corrector wedge [personal communication]," 01-Oct-2018.

[51] "Optech Titan Product Page." [Online]. Available: https://www.teledyneoptech.com/en/products/airborne-survey/titan/. [Accessed: 15-Jun-2019].

[52] C. A. Ogaja, *Applied GPS for Engineers and Project Managers*. Reston, VA: American Society of Civil Engineers, 2011.

[53] T. Soler, Ed., *CORS and OPUS for Engineers: Tools for Surveying and Mapping Applications*. Reston, VA: American Society of Civil Engineers, 2011.

[54] G. Wang, "Teaching High-Accuracy Global Positioning System to Undergraduates Using Online Processing Services," *Journal of Geoscience Education*, vol. 61, no. 2, pp. 202–212, May 2013.

[55] C. R. Schwarz, R. A. Snay, and T. Soler, "Accuracy assessment of the National Geodetic Survey's OPUS-RS utility," *GPS Solutions*, vol. 13, no. 2, pp. 119–132, Mar. 2009.

[56] R. Snay, K. Choi, G. Mader, C. Schwarz, T. Soler, and N. Weston, "How precise is OPUS? Part 3: The rest of the story," *The American Surveyor*, vol. 8, no. 5, 2011.

[57] W. Böhler, M. Bordas Vicent, and A. Marbs, "Investigating laser scanner accuracy," in *XIXth CIPA Symposium, Antalya, Turkey*, 2003.

[58] P. Axelsson, "DEM generation from laser scanner data using adaptive tin models," *International Archives of Photogrammetry and Remote Sensing*, vol. XXXIII, no. 4, pp. 110–109, 2000.

[59] W. Zhang, J. Qi, P, Wan, H. Wang, D. Xie, X. Wang, G. Yan, "An Easy-to-Use Airborne LiDAR Data Filtering Method Based on Cloth Simulation," *Remote Sensing*, vol. 8, no. 6, p. 501, Jun. 2016.

[60] D. Freedman, R. Pisani, and R. Purves, *Statistics*, 3rd ed. W. W. Norton & Company, 1997.

[61] J. Devore, *Probability and Statistics for Engineering and the Sciences*, 7th ed. Thomson Brooks/Cole, 2007.

[62] A. G. Kashani, M. J. Olsen, C. E. Parrish, and N. Wilson, "A Review of LIDAR Radiometric Processing: From Ad Hoc Intensity Correction to Rigorous Radiometric Calibration," *Sensors (Basel)*, vol. 15, no. 11, pp. 28099–28128, Nov. 2015.

[63] W. Wagner, "Radiometric calibration of small-footprint full-waveform airborne laser scanner measurements: Basic physical concepts," *ISPRS Journal of Photogrammetry and Remote Sensing*, vol. 65, no. 6, pp. 505–513, Nov. 2010.

[64] T. Schulz, "Calibration of a terrestrial laser scanner for engineering geodesy," Doctoral Thesis, ETH Zurich, 2008.

[65] M. Zámečníková, A. Wieser, H. Woschitz, and C. Ressl, "Influence of surface reflectivity on reflectorless electronic distance measurement and terrestrial laser scanning," *Journal of Applied Geodesy*, vol. 8, no. 4, pp. 311–326, 2014.

[66] D. Wujanz, M. Burger, M. Mettenleiter, and F. Neitzel, "An intensity-based stochastic model for terrestrial laser scanners," *ISPRS Journal of Photogrammetry and Remote Sensing*, vol. 125, pp. 146–155, Mar. 2017.

[67] E. P. Baltsavias, "Airborne laser scanning: basic relations and formulas," *ISPRS Journal of Photogrammetry and Remote Sensing*, vol. 54, no. 2, pp. 199–214, Jul. 1999.

[68] J. R. Schott, *Remote Sensing: The Image Chain Approach*, Second Edition. Oxford, New York: Oxford University Press, 2007.

[69] Z. Pan, "SPL100 noise filtering [personal communication]," 22-Jul-2019.

Abbreviations

AGL - Above Ground Level

ALS - Airborne Laser Scanning

APD - Avalanche Photodiode

CFD - Constant Fraction Discriminator

CSF - Cloth Simulation Filtering

FOV - Field of View

FWHM- Full-Width Half-Maximum

GmAPD - Geiger-Mode Avalanche Photodiode

GML - Geiger-Mode Lidar

GNSS - Global Navigation Satellite System

GPS - Global Positioning System

HRQLS - High-Resolution Quantum Lidar System

IFOV – Instantaneous Field of View

IMU - Inertial Measurement Unit

Lidar - Light Detection and Ranging

LML - Linear Mode Lidar

MCP-PMT - Microchannel Plate Photomultiplier Tube

MPL - Multiphoton Lidar

NCALM - The National Center for Airborne Laser Mapping

NIR - Near-infrared

PMT - Photomultiplier Tube

PRF - Pulse Repetition Frequency

SiPM - Silicon Photomultiplier

SNR – Single to Noise Ratio

SPL - Single Photon Lidar

TOF - Time of Flight

Appendix

Table 8: OPUS-RS Output Report Values

Survey	Latitude RMS (cm)	Longitude RMS (cm)	Ellip Height RMS (cm)	% Observations Used	Quality Index	Quality Index
1	1.0	0.8	3.7	82	7.21	46.55
2	1.0	0.8	3.3	92	8.40	40.40
3	0.9	0.8	1.6	81	16.87	47.13
4	1.2	0.9	1.9	74	18.12	14.43
5	1.3	0.9	3.6	63	20.85	22.30
6	1.4	0.9	3.4	82	4.18	37.20
7	1.1	0.7	2.3	88	26.61	68.82
8	1.1	0.7	3.7	89	23.29	58.62
9	1.3	0.8	2.8	80	19.08	42.48
10	1.3	0.8	2.8	76	16.09	34.39
11	1.4	0.7	2.3	72	19.28	41.46
12	1.2	0.7	1.9	71	25.56	47.28
13	1.2	0.7	2.1	72	24.14	42.99
14	1.0	0.8	2.3	91	14.99	38.69
15	1.1	0.7	3.3	87	21.05	37.38
16	1.2	1.2	2.6	81	12.46	31.96
17	1.0	1.5	3.7	50	17.50	11.51
18	Unable to process			N/A	N/A	N/A
19	1.1	0.6	2.4	81	19.56	44.46
20	1.1	0.8	3.9	76	10.79	23.75
21	1.6	0.9	6.2	43	6.90	12.09
22	1.6	1.5	7.2	68	4.12	11.09
23	0.9	0.7	4.2	76	12.31	51.61
24	0.9	0.7	6.1	73	11.81	47.04
25	1.2	1.5	5.0	75	10.40	33.56
26	1.4	1.2	2.9	88	8.66	30.22
27	0.9	0.6	5.0	90	12.21	17.67
28	1.1	1.0	5.5	67	15.39	30.83
29	1.2	0.6	5.2	69	17.71	33.28
30	1.3	0.6	5.5	73	17.05	21.77
31	0.8	0.7	6.9	79	19.09	29.75
32	0.7	0.7	3.5	85	7.62	2.85
33	1.0	1.0	6.8	98	7.47	24.94
34	1.1	0.9	3.6	100	5.69	45.90
35	1.2	0.6	4.0	80	19.76	34.85
MEAN	**1.1**	**0.9**	**3.9**	**78**	**14.77**	**34.10**

Table 9: OPUS-RS and GrafNet, Final Results

Survey	Latitude RMS (cm)	Longitude RMS (cm)	Ellip Height RMS (cm)
1	1.0	0.8	3.7
2	1.0	0.8	3.3
3	0.9	0.8	1.6
4	1.2	0.9	1.9
5	1.3	0.9	3.6
6	1.4	0.9	3.4
7	1.1	0.7	2.3
8	1.1	0.7	3.7
9	1.3	0.8	2.8
10	1.3	0.8	2.8
11	1.4	0.7	2.3
12	1.2	0.7	1.9
13	1.2	0.7	2.1
14	1.0	0.8	2.3
15	1.1	0.7	3.3
16	1.2	1.2	2.6
17	1.0	1.5	3.7
18	Unable to process		
19	1.1	0.6	2.4
20	1.1	0.8	3.9
21	0.5	0.5	0.6
22	0.5	0.5	0.6
23	0.5	0.5	0.6
24	0.5	0.5	0.6
25	0.5	0.5	0.6
26	1.4	1.2	2.9
27	0.5	0.5	0.7
28	0.5	0.5	0.7
29	0.5	0.5	0.7
30	0.5	0.5	0.7
31	0.5	0.5	0.6
32	0.5	0.5	0.6
33	1.0	1.2	3.2
34	0.9	1.0	2.0
35	1.2	0.6	4.0
MEAN	**1.0**	**0.8**	**2.1**

Table 10: Positional Accuracy for Optech Titan

Survey	Δ Easting (cm)	Δ Northing (cm)	Δ Ellipsoidal (cm)
1	14.40	10.30	-12.90
2	-6.10	18.60	-16.50
3	-12.40	27.10	-12.10
4	-21.00	-13.40	-19.50
5	-8.00	18.70	-11.90
6	-17.20	-0.30	-12.90
7	11.30	-10.40	-24.10
8	8.70	25.10	-21.00
9	5.70	29.10	-18.30
10	7.00	20.00	-11.50
11	16.30	23.10	-15.10
12	-37.50	35.70	-4.50
13	5.20	-1.00	7.50
14	6.40	23.70	-13.10
15	-3.00	3.10	-13.60
16	-11.00	25.80	-13.90
17	5.30	13.90	-9.10
18	24.50	9.80	-18.90
19	17.50	21.30	-16.00
20	35.63	-0.98	-26.65
21	14.75	-8.55	-17.04
22	-17.83	8.26	-11.45
23	0.40	35.53	-14.22
24	27.70	2.00	-23.70
25	-4.56	8.34	-10.97
26	-5.27	-10.18	-11.83
27	-27.18	3.26	-10.98
28	35.78	-7.86	-15.93
29	-14.79	36.77	-12.13
30	11.72	13.78	-10.02
31	-25.28	-11.37	12.92
32	-12.20	36.10	-12.20
33	-10.20	29.80	-16.40
MEAN	0.45	12.58	-13.27
STD DEV	17.83	15.60	7.63

Table 11: Positional Accuracy for SPL100

Survey	Δ Easting (cm)	Δ Northing (cm)	Δ Ellipsoidal (cm)
1	3.40	-11.70	12.10
2	-25.10	-9.40	12.50
3	2.60	8.10	10.90
4	-8.00	-11.40	6.50
5	-18.00	4.70	12.10
6	-20.20	-2.30	15.10
7	-9.70	-0.40	14.90
8	12.70	13.10	5.00
9	-1.30	-1.90	0.70
10	9.00	4.00	6.50
11	4.30	-7.90	9.90
12	9.50	3.70	11.50
13	7.20	4.00	18.50
14	-7.60	11.70	5.90
15	-2.00	-2.90	12.40
16	-2.00	-16.20	14.10
17	4.30	3.90	19.90
18	7.50	-1.20	4.10
19	11.50	12.30	16.00
20	-4.37	8.02	-8.65
21	-5.25	5.45	19.96
22	-2.83	7.26	9.55
23	-9.60	-6.47	2.78
24	7.70	6.00	5.30
25	-5.56	-13.66	22.03
26	-5.27	-5.18	18.17
27	-33.18	-33.74	14.02
28	5.78	-14.86	16.07
29	0.21	20.77	12.87
30	-0.28	-1.22	4.98
31	-19.28	-1.37	35.92
32	7.80	-12.90	4.80
33	-10.20	-0.20	18.60
MEAN	-2.92	-1.27	11.67
STD DEV	11.00	10.68	7.88

Table 12: Canopy Penetration Statistics for Optech Titan (LML)

Sample	Area (m^2)	Percent of Pulses Reaching Ground (%)	Percent of Pulses with Multiple Returns (%)
1	362.8	91.5	98.7
2	496.5	86.7	92.1
3	472.8	80.2	90.0
4	595.1	60.5	80.2
5	483.7	58.7	82.5
6	393.6	72.3	85.2
7	333.6	67.0	85.4
8	385.4	76.5	86.0
9	455.0	63.4	73.9
10	1,189.8	76.1	88.2
11	893.0	78.7	89.3
12	480.8	88.1	91.2
13	603.0	77.4	86.4
14	515.6	75.1	84.2
15	894.5	67.8	82.7
16	786.7	52.4	74.8
17	684.4	58.3	79.3
18	1,282.8	59.5	82.5
19	4,830.4	56.1	86.7
20	1,778.4	59.2	84.3
21	1,109.8	96.6	91.8
22	1,174.9	78.3	87.7
23	2,025.9	71.5	82.4
24	1,135.8	92.1	93.0
25	5,231.1	76.6	86.8
26	1,560.9	79.2	89.2
27	1,182.1	86.9	89.5
28	3,069.6	81.8	89.3
29	858.0	84.3	88.9
30	1,307.1	95.2	88.6
	MEAN	74.9	86.4
	STD DEV	12.4	5.2

Table 13: Canopy Penetration Statistics for Leica SPL100

Sample	Area (m^2)	Percent of Pulses Reaching Ground (%)	Percent of Pulses with Multiple Returns (%)
1	360.3	53.1	35.7
2	491.0	48.8	24.9
3	470.9	50.3	22.9
4	597.2	31.5	16.9
5	406.8	31.0	18.9
6	393.9	38.5	21.6
7	338.1	49.4	21.3
8	249.9	52.8	20.9
9	448.9	43.1	19.7
10	1,198.3	42.1	23.0
11	885.7	48.2	23.4
12	482.8	40.8	21.6
13	602.7	46.0	20.9
14	513.9	39.7	17.7
15	904.2	46.2	23.9
16	784.3	26.2	13.7
17	413.3	45.1	19.2
18	1,354.3	14.9	6.4
19	4,845.2	17.2	11.9
20	1,803.6	14.7	9.6
21	1,182.4	70.6	22.9
22	1,167.8	46.5	14.2
23	2,019.8	59.2	23.6
24	1,132.6	66.6	23.1
25	5,217.0	41.7	23.5
26	1,548.1	37.8	19.8
27	1,195.6	61.2	30.4
28	3,051.1	58.3	14.1
29	854.3	54.1	21.9
30	1,295.2	72.9	15.9
	MEAN	44.9	20.1
	STD DEV	14.8	5.8